Epithelial cells adapt to curvature induction via transient active osmotic swelling

Caterina Tomba, Valeriy Luchnikov, Luca Barberi, Carles Blanch-Mercader,
Aurélien Roux

HAL Id: hal-03678923
https://hal.science/hal-03678923

Submitted on 25 May 2022

Epithelial cells adapt to curvature induction via transient active osmotic swelling

Graphical abstract
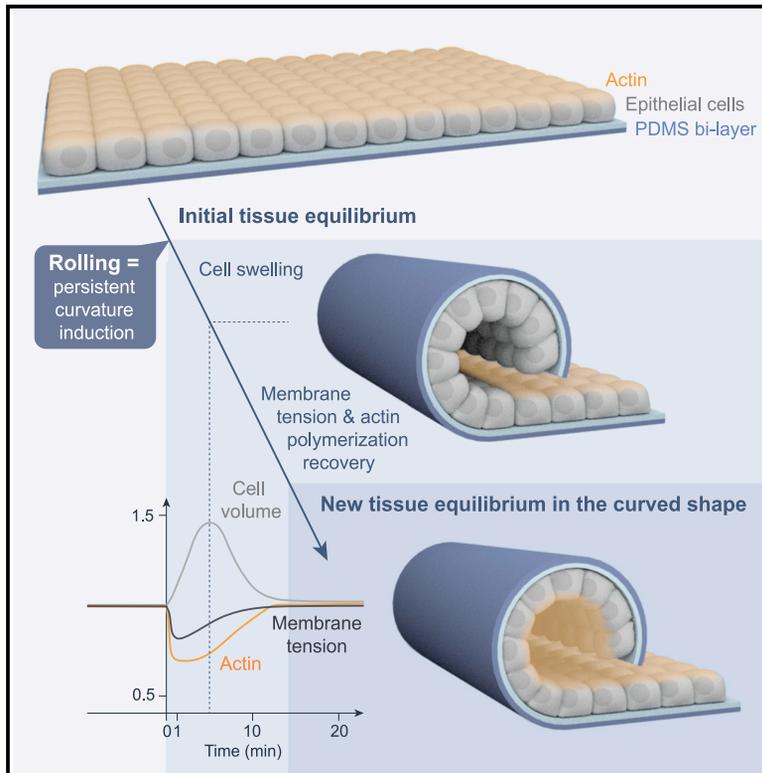
Authors

Caterina Tomba, Valeriy Luchnikov,
Luca Barberi, Carles Blanch-Mercader,
Aurélien Roux

Correspondence

caterina.tomba@univ-lyon1.fr (C.T.),
aurelien.roux@unige.ch (A.R.)

In brief

Tomba et al. examine the response of epithelial cells to rapid changes in curvature. They show that upon curvature induction, cell volume transiently increases while membrane tension decreases and actin depolymerizes. Actin repolymerization and membrane tension recovery restore cell volume and forces in the new curved configuration.

Highlights

- Rapid inward and outward epithelial rolling triggers cell volume increase

- Epithelial folding induces a mechano-osmotic feedback loop that involvs ion channels

- Cell volume regulation in curved tissues involves actin, membrane tension, and mTORC2

CellPress

Article

Epithelial cells adapt to curvature induction via transient active osmotic swelling

Caterina Tomba,[1,4,*] Valeriy Luchnikov,[2] Luca Barberi,[1] Carles Blanch-Mercader,[1,5] and Aurélien Roux[1,3,6,*]

[1]Department of Biochemistry, University of Geneva, Quai Ernest Ansermet 30, Geneva 1211, Switzerland
[2]Université de Haute Alsace, CNRS, IS2M UMR 7361, 15, rue Jean Starcky, Mulhouse 68100, France
[3]National Center of Competence in Research Chemical Biology, University of Geneva, Quai Ernest Ansermet 30, Geneva 1211, Switzerland
[4]Present address: Univ Lyon, CNRS, INSA Lyon, Ecole Centrale de Lyon, Université Claude Bernard Lyon 1, CPE Lyon, INL, UMR5270, Villeurbanne 69622, France
[5]Present address: Laboratoire Physico Chimie Curie, UMR 168, Institut Curie, PSL Research University, CNRS, Sorbonne Université, 75005 Paris, France
[6]Lead contact
*Correspondence: caterina.tomba@univ-lyon1.fr (C.T.), aurelien.roux@unige.ch (A.R.)
https://doi.org/10.1016/j.devcel.2022.04.017

SUMMARY

Generation of tissue curvature is essential to morphogenesis. However, how cells adapt to changing curvature is still unknown because tools to dynamically control curvature *in vitro* are lacking. Here, we developed self-rolling substrates to study how flat epithelial cell monolayers adapt to a rapid anisotropic change of curvature. We show that the primary response is an active and transient osmotic swelling of cells. This cell volume increase is not observed on inducible wrinkled substrates, where concave and convex regions alternate each other over short distances; and this finding identifies swelling as a collective response to changes of curvature with a persistent sign over large distances. It is triggered by a drop in membrane tension and actin depolymerization, which is perceived by cells as a hypertonic shock. Osmotic swelling restores tension while actin reorganizes, probably to comply with curvature. Thus, epithelia are unique materials that transiently and actively swell while adapting to large curvature induction.

INTRODUCTION

Many morphogenic events are characterized by epithelium folding: gastrulation (Burke et al., 1991; Sweeton et al., 1991), neurulation (Schoenwolf and Smith, 1990), and villification of the intestine (Chin et al., 2017) are driven by cell shape changes caused by changes of cell surface tension such as apical constriction (Kim et al., 2013; Martin and Goldstein, 2014; Sawyer et al., 2010). Cell surface tension results from plasma membrane tension, acto-myosin contractility, and cell-cell and cell-substrate adhesion forces (Lecuit and Lenne, 2007), and it is thus a major regulator of morphogenesis. At a shorter time-scale, tissues have to often rapidly adapt to large deformations and folding due to activities of the organs external to the tissue. For instance, the intestinal villi during peristalsis, the lung alveoli during breathing, and skin wrinkling during muscular contraction. Several works investigated epithelial tissue response to in-plane or out-of-plane stretching or compression, both *in vitro* and *in vivo* (Brunette, 1984; Duda et al., 2019; Gérémie et al., 2022; Harris et al., 2012; Streichan et al., 2014), and only recent studies analyzed cell response to induced tension and torque in folding epithelia (Blonski et al., 2021) or to induced buckling in compressed tissues (Trushko et al., 2020; Wyatt et al., 2020).

Folding forms buckled shapes that are predicted by mechanical models (Rauzi et al., 2013) and are produced by several processes: proliferation under externally imposed confinement (Trushko et al., 2020), differences in proliferation between domains of the same tissue (Hong et al., 2018; Tozluoğlu et al., 2019), or active contractility of muscles around a growing intestinal epithelium (Shyer et al., 2013). Thus, mechanical stresses emerging in reaction to external constraints are determinants of epithelium folding. However, very little is still known about how tissues respond in time to external mechanical stresses. Cell monolayers under compression maintain their cell density constant through time by increasing cell extrusion and reducing cell proliferation (Eisenhoffer et al., 2012). Opposite reactions are seen upon tissue stretching (Gudipaty et al., 2017; Streichan et al., 2014). These results concern flat tissues and do not address how cells react to changes in the three-dimensional (3D) tissue organization, in particular, to changes in their curvature.

Curved substrates have been developed for cell culture (Baptista et al., 2019) to study curvotaxis (Callens et al., 2020), a term that designates all processes guided by curvatures such as cell shape, motility, adhesion, and gene expression. For instance, concave surfaces orient cell polarity and cell migration (Bade et al., 2018; Pieuchot et al., 2018), increasing migration speed

by reducing contacts with the substrate (Werner et al., 2017). In contrast, convex regions enhance osteogenic differentiation by modulating cytoskeleton forces acting on the nucleus (Werner et al., 2017). At a multi-cellular scale, curvature controls actomyosin contractility during tissue growth (Bidan et al., 2018), epithelium detachment from concave regions (Maechler et al., 2019; Yamashita et al., 2016), and collective migration inside and outside of cylindrical substrates (Xi et al., 2017; Yevick et al., 2015). All these curvature and actin-dependent cell processes require to integrate local cell constraints over long distances through cell-cell and cell-substrate adhesions (Broaders et al., 2015). However, all these studies investigate cells adhering to substrates with fixed curvature, whereas *in vivo*, they experience forces and curvatures that are constantly changing.

To study how tissues would react to induction of curvature, we looked for techniques that could acutely change the curvature of the substrate onto which cells would have been grown. The engineering of controlled strain gradients in nanomembranes leading to the self-rolling of thin solid films (Kumar et al., 2009; Mei et al., 2008) offered a versatile strategy to produce complex 3D structures for a large panel of applications in flexible electronics, soft robots, and biomedical devices (Cheng and Zhang, 2019; Luchnikov et al., 2011). This approach was recently used in biomimetic self-folding macro-structures, based on anisotropic swelling of printed hydrogel composites (Gladman et al., 2016). Biocompatible micro-containers were developed to control drug release (Egunov et al., 2016a; Jamal et al., 2013), to encapsulate cells in rolled films for potential implantable tissue grafts (Teshima et al., 2017), or to mimic blood vessels and muscle fibers (Yuan et al., 2012). These bioengineering technologies (Ionov, 2018) proved cell viability on scaffolds that spontaneously change their shape (Feiner et al., 2016). Here, we present a self-rolling elastomer thin film that forces a cell monolayer to fold into a tubular shape.

RESULTS

Curvature induction of epithelial monolayers by rolling their supporting substrate

We prepared self-rolling substrates according to the fabrication process reported in Figure 1A. The technique is based on the built-in spontaneous curvature of a polydimethylsiloxane (PDMS) film (Egunov et al., 2016b), which presents the advantage of creating anisotropic curvature and provides an internal control, as the PDMS film does not roll over parts strongly adhering to the bottom substrate. It consists of a superposition (from bottom to top) of a PDMS layer on a glass slide, a gelatin film circumscribed to the central part of the PDMS layer below, and finally a bilayer of two different PDMS composites: the top leaflet of PDMS contains silicon oil, and it is strongly adherent to the bottom, oil-free PDMS leaflet. Oil extraction is performed through immersion of the whole substrate in isopropanol, forming a pre-constrained PDMS bilayer, which spontaneously rolls in less than 10 s when cut over the gelatin (Egunov et al., 2016b). The PDMS bilayer adheres to the bottom PDMS outside the gelatin patch, keeping it flat until cut.

To confine cell adhesion, a delimited area is activated by plasma surface treatment and then coated with fibronectin. We employed Madin-Darby canine kidney (MDCK) cells that form well-organized epithelial layers, whose cell mechanics and collective behavior are among the best described. Cells were let to adhere and form a polarized monolayer for 24 h. Finally, by cutting the PDMS bilayer and consequently the cell monolayer adhering to its top surface, the pre-constrained PDMS bilayer is allowed to roll (Figure 1A; Video S1).

Multi-rolls were discarded because cells may be squeezed between two (or more) roll layers, adding an undesired constraint (Figure S1A). Thus, we optimized the formation of single roll tubes (Figures 1B and 1C) by reducing the region covered by gelatin (down to a 0.5 cm width) and limiting the cut length (up to 1.5 cm). As the radius of curvature is proportional to the substrate thickness (Egunov et al., 2016b), we fixed a PDMS bilayer thickness of $14 \pm 1 \mu m$ (Figures S1B and S1C) that produces the relevant curvature radii (Figure 1D) found *in vivo*, such as the lung alveoli (Yablonskiy et al., 2002), the intestinal villi (Sankar et al., 2013), or the glomeruli in the kidney (Kotyk et al., 2016). We observed that the tube radii were maintained constant over time (Figure S1D), suggesting a constant constraint on the cell monolayer. Using a simple elastic model (Methods S1), we estimated that the substrate exerts a pressure of ~ 4 Pa onto the monolayer while imposing its preferred radius of curvature. The cell monolayer is not expected to significantly unroll the PDMS substrate, given that it is much less rigid than the PDMS. In particular, we predicted that the relative deviation of the tube radii from the optimal radius of curvature of the substrate due to the elastic resistance of the cell monolayer is in the order of 4% (Methods S1).

Moreover, we estimated the change of thickness of the PDMS bilayer and of the epithelial cells upon rolling (Methods S2). If purely incompressible (constant volume), the cells are expected to thicken by 25% and decrease their width by 20%. If the cells are compressible, their volume should decrease by $\sim 5\%$ (Methods S1). We then investigated these predictions.

Cells actively respond to curvature by increasing their volume

First, we analyzed changes in cell shape upon rolling. To combine high statistics, a time resolution of few minutes after rolling, and high-resolution imaging, cells were chemically fixed with 4% paraformaldehyde (PFA) at different time points after rolling. By 3D segmentation (STAR Methods), we quantified the average cell volume over time, both in planar and tubular regions (Figure 2A). Cell volumes and shapes on flat PDMS do not change after fixation, showing that PFA does not affect our analysis (Figures S2A and S2B).

Orthogonal views of the cell monolayer showed that cell thickness increased and peaked at 5 min after rolling (Figure 2B), whereas the cell width stayed constant (Figure 2C). This cell shape change led to a mean aspect ratio (height/width) of 1.40 ± 0.47 at 5 min compared with 1.03 ± 0.23 on flat regions (Figure S2C). Thus, the resulting cell thickening is higher and delayed in time compared with the maximum value of 25% predicted for a rolled incompressible epithelium (Methods S2). Moreover, the cell apical pole, which is normally very flat (Figure 2F), appeared swollen (Figure 2E). This was associated with a volume increase up to $\sim 40\%$ at 5 min (Figures 2D and 2E) compared with cell volume on flat regions (Figures 2D and 2F). This volume increase is fully consistent with the observed
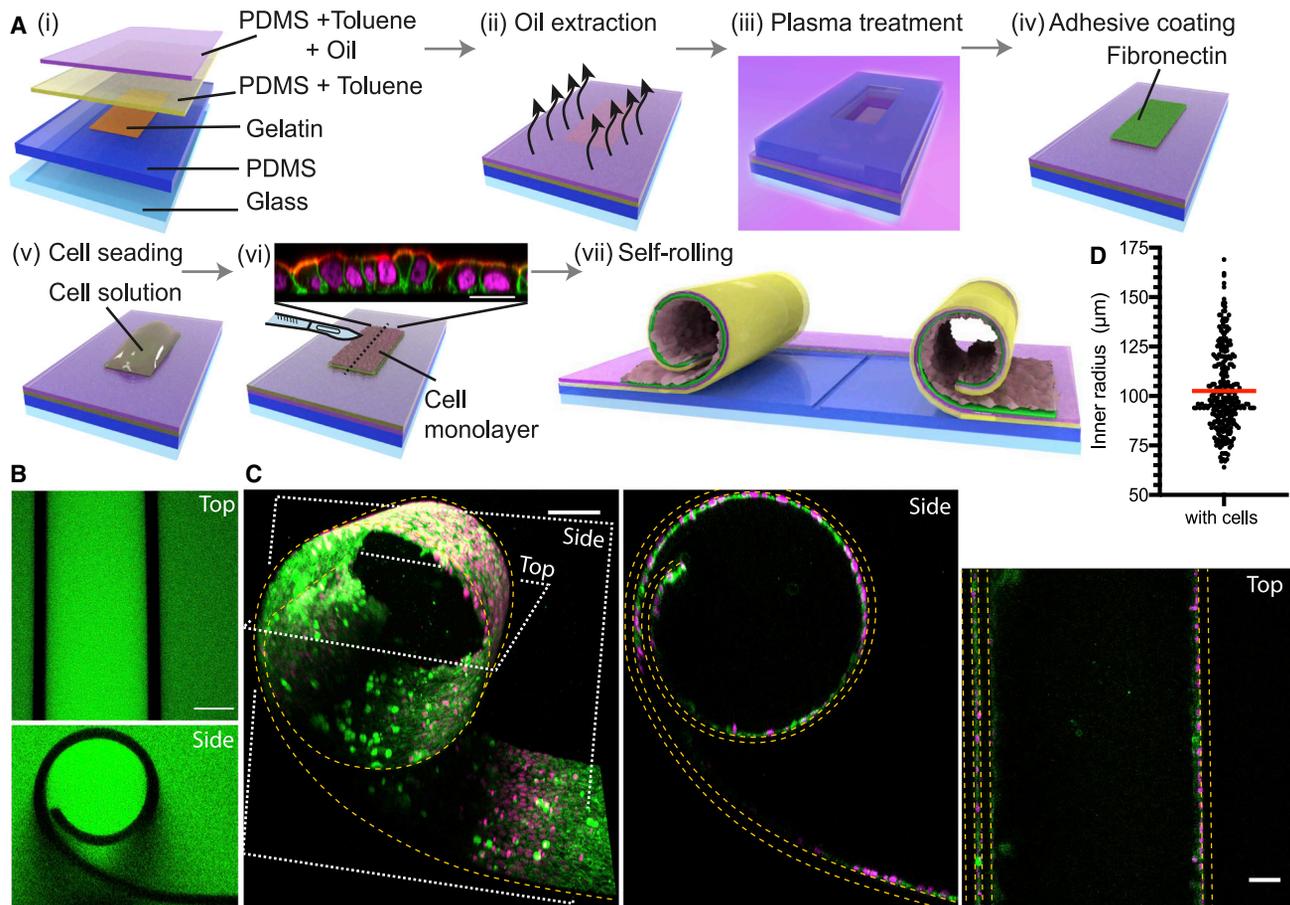
Figure 1. Self-rolling substrates induce cylindrical deformation of epithelial cell monolayers

(A) Schematic of concave curvature generation on a (Ai) multi-layer substrate composed of: glass slide (light blue); PDMS sheet (dark blue); central gelatin patch (brown); bottom PDMS leaflet and toluene solution (yellow); top leaflet of PDMS, toluene, and silicon oil solution (pink); (Aii) oil extraction by isopropanol bath and formation of the strain gradient; (Aiii) surface activation by plasma treatment on the central region through a PDMS mask; (Aiv) fibronectin solution (green) incubation on the central region; (Av) cell solution (light pink) incubation; (Avi) substrate cutting after cell monolayer formation (inset: orthogonal view of a polarized cell layer, ezrin [red], cell membrane [Myr-Palm-GFP, green], and nuclei [H2B-mCherry, magenta]. Scale bars, 20 μm); (Avii) self-rolling of the substrate upon cutting.

(B) Top (top) and side (bottom) views of a PDMS tube without cells, dextran solution (green). Scale bars, 50 μm.

(C) 3D view (left, scale bars, 100 μm), side (middle) and top (right) views (scale bars, 50 μm) of a PDMS tube with cells, cell membrane (deep-red CellMask, green), and nuclei (H2B-mCherry, magenta).

(D) Distribution of inner radii of tubes with cells. The red line stands for the mean value, n = 278 images, N of independent replicates = 3.

~40% increase in height without width reduction (Figures 2B and 2C). This is an unusual response of the material to bending constraints, observed in rare materials with negative compressibility such as some rear crystals (Baughman et al., 1998), polymer foams (Lakes and Wojciechowski, 2008), and bi-material ligaments (Gatt and Grima, 2008).

However, and different from materials with negative compressibility, the gradual increase was followed by a slow recovery to the normal volume within 20 min, suggesting that the response and its recovery were active (energy-consuming) cell processes. Other than volume increase, we observed no other striking change in cell shape. We observed neither cell displacements (Video S2) nor cell shape elongation in the axis of the tube (Figure S2D) nor increased cell extrusion (Video S3).

To test if the volume increase and its recovery were active responses to curvature, we first investigated the deformation of

cells chemically fixed before rolling. No cell volume increase was observed in this case (Figure 2G), confirming that epithelial cells actively increased their volume upon rolling. This result also confirmed that the volume increase observed after rolling in living cells was not resulting from the roll geometry altering the quantification of cell volumes. We then wondered whether the response could be induced by compressive or stretching stresses occurring upon curvature induction. We estimated the theoretical compression of the PDMS layer upon rolling to be less than ~15% (Methods S3). We used mechanical stretchers to produce cell compression and stretching while the overall shape of the epithelium stayed flat. To apply compression, cells were grown on a pre-stretched PDMS layer by ~15%, which was then released. Inversely, to produce stretching, cells grew on a PDMS layer that was then stretched by ~15% (Figure 2H). Stretching and compression of the substrate were performed
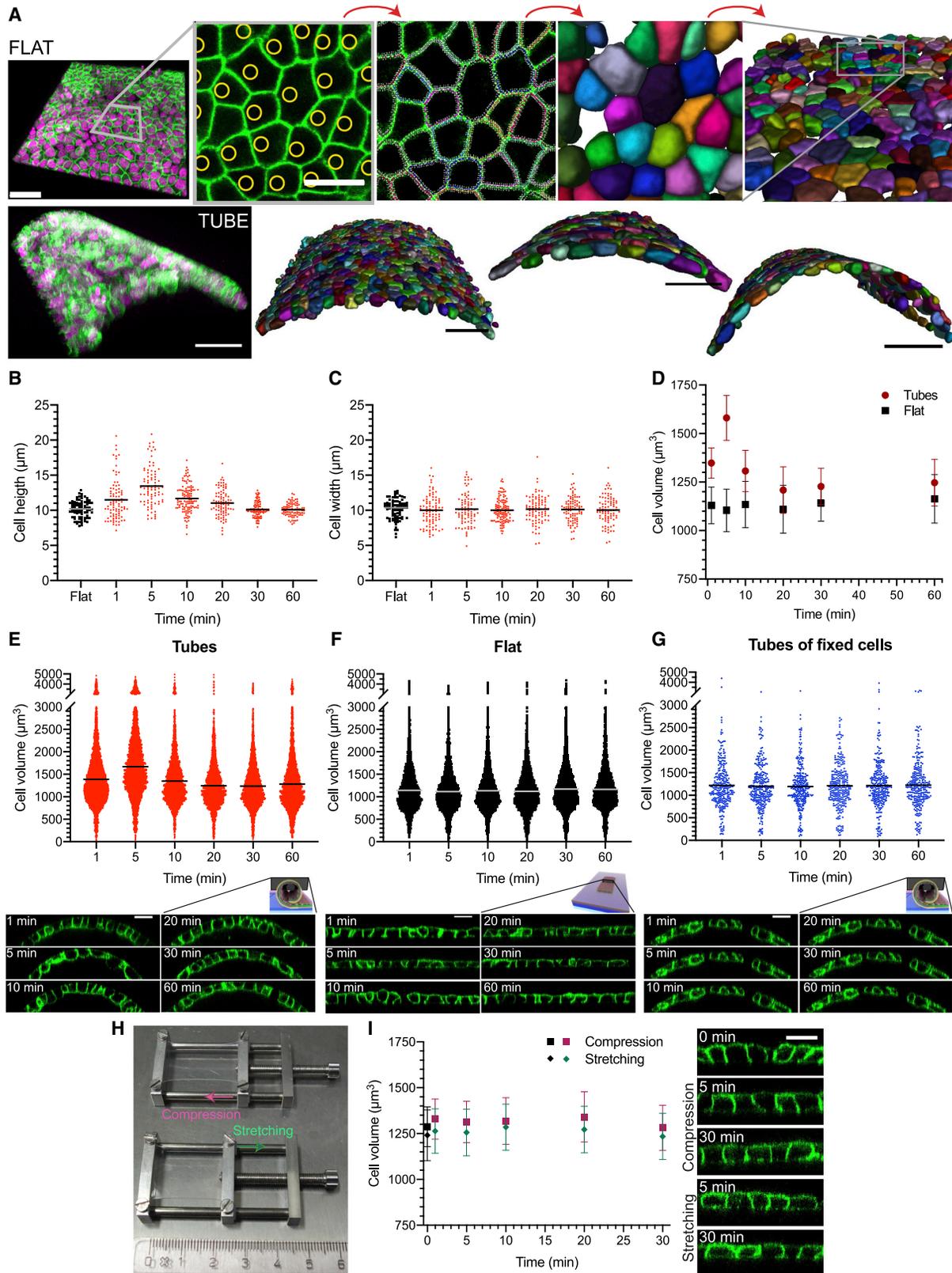
Figure 2. Cell volume increase and recovery are an active response

(A) Cell volume measurements. Top, from left to right: 3D view of a cell monolayer on a flat PDMS substrate (scale bars, 50 μm); centroid identification of the nuclei (yellow circles) by segmentation (scale bars, 20 μm); 3D cell membrane segmentation; 3D reconstruction of cell shapes (zoom and large views, random colors

in less than 10 s, thus as fast as rolling. In both conditions, cell volume stayed constant over time (Figures 2I and S2E), supporting that cell volume increase was specific to curvature induction.

Finally, we confirmed that cell volume stayed constant after cutting a flat epithelium, implying that cell volume increase was not a consequence of damage to the cells (Figures S2F and S2G). Altogether, our results show that the transient cell volume increase is an active response to a rapid change of curvature.

Cell volume increases are independent of the sign of the curvature

Next, we wondered which parameters of curvature could directly impact the cell response. As shown in Figure 1D, the mean curvature radius obtained in the tubes with a cell monolayer was 102.7 ± 20.9 μm. Interestingly, at around 5 min, the peak of cell volume occurred independently of the curvature radii, as long as it was below a threshold radius of ~180 μm (Figures S3A and S3B). Density also affected the volume change, and as for half seeding densities, the cell volume remained constant (Figures S3C–S3E), suggesting that volume increase depended on cell compaction.

Surface curvature has two possible orientations (convex versus concave), and we wondered if both orientations could produce a similar volume increase. To roll the PDMS bilayer in the other orientation, we inverted the order of the two PDMS leaflets (Figure 3A). With this approach, the curvature radii obtained were larger (Figure 3B). However, we still observed a cell volume increase upon substrate rolling (Figure 3C), associated with apical height increase (Figure 3D) and recovery within 20 min. Thus, in rolls, whether the induced curvature is positive or negative, it triggers the same active response of the epithelium, i.e., a transient increase in cell volume.

In rolls, the curvature is the same over long distances. Thus, we wondered how the response of the epithelium would be when both curvatures are induced on the same substrate. To do this, we took advantage of a technique that we recently developed to produce wavy substrates (Tomba et al., 2019). First, a thin hard layer at the surface of a prestrained elastomer is formed by infrared laser irradiation, which then spontaneously adopts a wrinkled morphology upon stress relaxation (Figure 3E). The radii of curvature obtained with this technique (Figure 3F) are locally smaller than the values given by the self-rolling substrates (Figures 1D and 3B). We first grew cells until confluence on flat

pre-stretched and irradiated substrates and relaxed the substrate to form the wrinkles. Then, the cells were chemically fixed and segmented at different time points after wrinkling. We quantified cell volumes in the concave and convex regions (Figure 3G) and observed that they did not change (Figures 3H and 3I). Although the cells in the concave regions looked highly deformed (Figure 3J), these regions were only a few tens of microns, supporting the notion that the same curvature has to be propagated over long distances to have a significant impact on cell volume. Furthermore, in wrinkles, the effect induced by positive curvature could be compensated by the surrounding negative curvature. Overall, our results show that the cell volume increase is a collective response to the induction of curvature over large spatial regions. Further investigations would be necessary to better characterize this aspect, in particular, using waves with larger radii of curvature directly comparable with tube radii and larger amplitudes producing larger regions with the same curvature.

Ion channels, actin cytoskeleton, and membrane tension are at the origin of the curvature-induced cell swelling

To find the cellular functions involved in cell volume increase after rolling (Figure 2), we looked at processes known to participate in cell volume regulation. We identified a number of ionic channels that are involved in volume regulation during osmotic shocks and beyond (Hoffmann et al., 2009), the cell cytoskeleton, and target of rapamycin complexes (TORC) 1&2 signaling, which are major players in cell volume and surface regulation (Eltschinger and Loewith, 2016). Not surprisingly, both the cytoskeleton and TORC1&2 are also part of the cell volume response to osmotic shocks (Delarue et al., 2018; Riggi et al., 2018).

We first inhibited volume-regulated anion channels (VRACs) (Jentsch, 2016) by treating cells with DCPIB (4-[(2-Butyl-6,7-dichloro-2-cyclopentyl-2,3-dihydro-1-oxo-1H-inden-5-yl)oxy]butanoic acid) (Decher et al., 2001). DCPIB-treated cells slowly increased their volume upon rolling but without reaching the peak observed in non-treated cells (Figure 2D). Only partial recovery was observed after 30 min (Figures 4A, 4B, S4A, and S4C–S4E). Other key cell volume regulators are the Na^+-H^+ exchangers (NHEs), whose activity was blocked by EIPA (ethylisopropyl amiloride). The inhibition of the NHEs, which are known to regulate volume increase (Vallés et al., 2015), led to

represent different cells). Bottom, from left to right: 3D view of a cell monolayer on the top region of a PDMS tube; 3 representative examples of 3D reconstructions of cell volume on PDMS tubes. Scale bars, 50 μm.

(B) Distribution of cell height on flat regions (black squares) over time and on tubes (red circles) over time after cutting, n ≥ 81 cells/time point, N ≥ 3.

(C) Distribution of cell width on flat regions (black squares) and on tubes (red squares) over time after cutting, n ≥ 81 cells/time point, N ≥ 3.

(D) Weighted means and standard error of the weighted mean (SEWM, with variance weights) of cell volume on flat regions (black squares) and on tubes (red circles) over time after cutting, n ≥ 13 images/time points, N ≥ 4. (E) Distribution of cell volume on tubes (red circles) over time after cutting, n ≥ 2,729 cells/time point, N ≥ 4.

(F) Distribution of cell volume on flat regions (black circles), n ≥ 3,224 cells/time point, N ≥ 4.

(G) Distribution of cell volume on tubes formed after cell fixation in PFA (blue circles) over time after cutting, n ≥ 279 cells/time point, N = 1. Insets in (E)–(G) representative orthogonal views of cells on tubes or flat regions (see diagrams) at different time points after cutting. Scale bars, 20 μm.

(H) Pictures of the stretchers in the initial position before compression (top) and stretching (bottom) of about 15% of the elastomer film. 1 small mark in the ruler, 1 mm.

(I) Weighted means and SEWM (with variance weights) of cell volume on an elastomer film before compression (black square) or stretching (black rhombus) and after compression (magenta squares) or stretching (green rhombuses) over time, n ≥ 14 images/time point, N ≥ 3. Scale bars, 20 μm. In all images, green represents cell membrane, Myr-Palm-GFP, and magenta represents nuclei, H2B-mCherry. N is the number of independent replicates; the horizontal lines stand for the mean values.
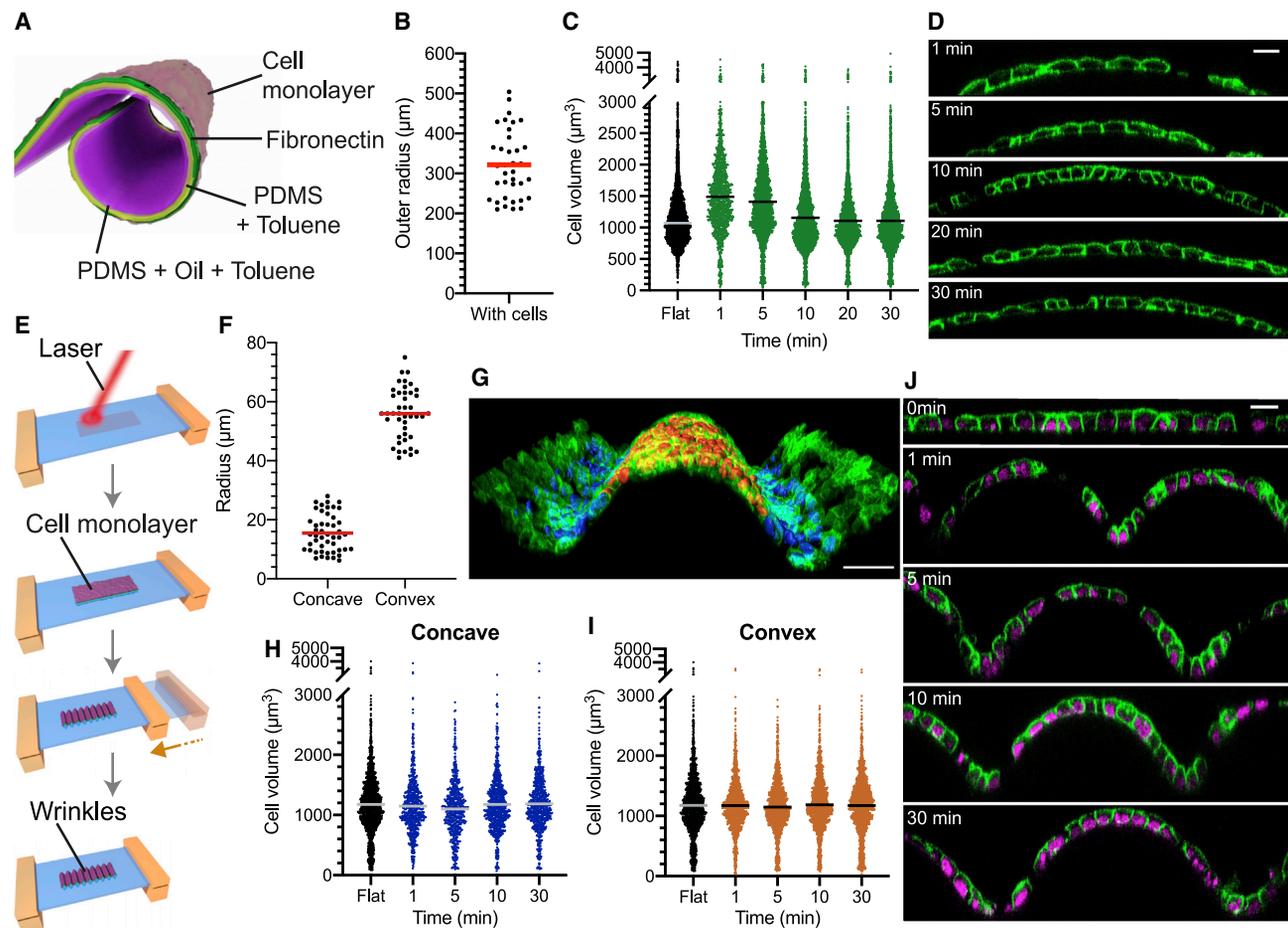
Figure 3. Both signs of curvature produce transient cell shape changes, but this effect is compensated on wavy substrates

(A) Schematic of convex curvature generation: PDMS and toluene with (pink) and without (yellow) silicon oil leaflets are inversed compared with Figure 1A. Fibronectin coating (green) and cell monolayer (light pink).

(B) Distribution of outer radii of tubes with cells, n = 36 images, N = 2.

(C) Distribution of cell volume on tubes with inverted sign of curvature (green circles) over time after cutting and before rolling (black circles), n ≥ 1,179 cells/time point, N = 3.

(D) Representative orthogonal views of cells on tubes with inverted sign of curvature at different time points after cutting. Scale bars, 20 μm.

(E) Schematic of wavy substrate formation. From the top: infrared laser exposure of the pre-stretched elastomer film; cell growth on the flat surface of the pre-stretched elastomer film; wavy morphologies formation at the surface from the stress relaxation of the substrate.

(F) Distribution of radii of the elastomer film in the concave and convex regions, n = 48 (concave) and 43 (convex) images, N = 1.

(G) 3D view of a representative cell monolayer on a wavy substrate; 3D reconstruction of segmented nuclei on the concave (blue) and convex (orange) regions. Scale bars, 50 μm.

(H) Distribution of cell volume on flat regions before substrate relaxation (black circles) and concave regions of wavy substrates (blue circles) over time after relaxation, n ≥ 602 cells/time point, N = 1.

(I) Distribution of cell volume on flat regions before substrate relaxation (black circles) and convex regions of wavy substrates (orange circles) over time after relaxation, n ≥ 1,240 cells/time point, N = 1.

(J) Representative orthogonal views of cells on flat and wavy regions at different time points after relaxation. Scale bars, 20 μm. In all images, green represents cell membrane, Myr-Palm-GFP, and magenta represents nuclei, H2B-mCherry. N is the number of independent replicates, the horizontal lines stand for the mean values.

a reduced volume increase upon rolling, which fully recovered after 30 min (Figures 4C, 4D, S4B, and S4F–S4H). We then used bumetanide to inhibit Na$^+$-K$^+$-2Cl$^-$ cotransporter channels (NKCCs), which maintain the cell osmotic balance. Bumetanide treatment not only caused a lower initial volume increase but also strongly affected the volume recovery (Figures 4E, 4F, and S4I). Similar results were obtained with furosemide, another common NKCC blocker (Figures S4J–S4L). We

concluded that ion channels were involved in both the initial volume increase after rolling and its recovery. Thus, we hypothesized that the transient cell volume increase could be osmotic. To test this possibility, we first applied hypotonic shocks on flat cell monolayers and probed if cell volume and membrane tension changed. To follow membrane tension, we employed a fluorescent lipid tension reporter (FliptR or Flipper-TR), a probe that reports changes in membrane tension by changing its
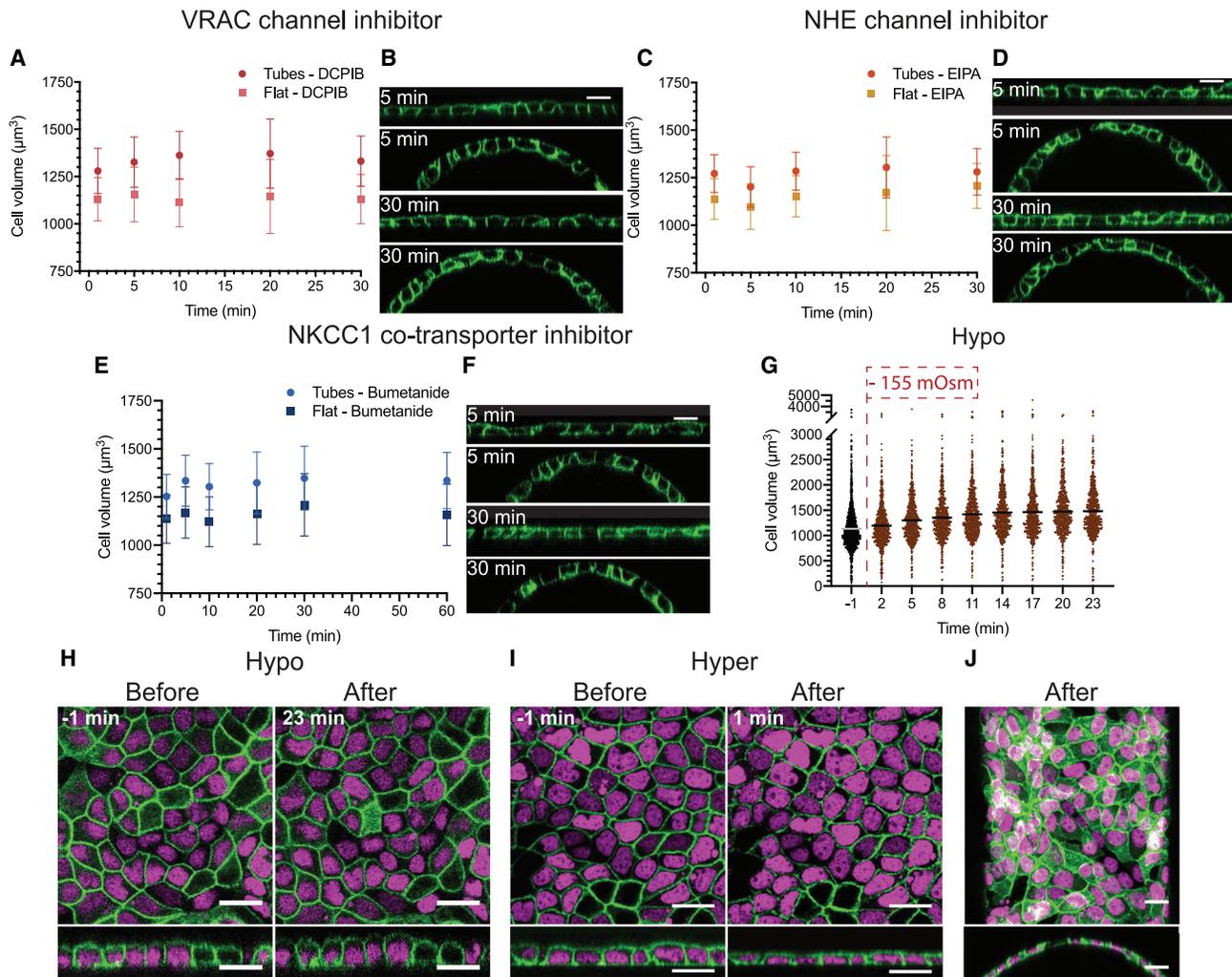
Figure 4. Ion channels regulate the osmotic balance perturbed by the change of curvature

(A–F) Weighted means and SEWM (with variance weights) of cell volume and representative orthogonal views on flat regions or tubes at 5 and 30 min after cutting of (A and B) DCPIB-treated cells on flat regions (light pink squares) and on tubes (dark pink circles) over time after cutting, n ≥ 6 images/time point, N = 3; of (C and D) EIPA-treated cells on flat regions (dark yellow squares) and on tubes (light orange circles) over time after cutting, n ≥ 6 images/time point, N = 3; and of (E and F) Bumetanide-treated cells on flat regions (dark blue squares) and on tubes (blue circles) over time after cutting, n ≥ 9 images/time point, N = 3.

(G) Distribution of cell volume on flat substrates before (black circles) and over time (minutes) after switching to a hypotonic solution ($\sim$−155 mOsm, brown circles), n ≥ 596 cells/time point, N = 1, the horizontal lines stand for the mean values.

(H) Representative images of cells on flat regions before and after hypoosmotic shock ($\sim$−155 mOsm), top (top) and side (bottom) views.

(I) Representative images of cells on flat regions before and after hyperosmotic shock ($\sim$+510 mOsm), top (top) and side (bottom) views.

(J) Representative images of cells on a tube after hyperosmotic shock ($\sim$+600 mOsm), maximum-intensity z-projection (top) and side (bottom) views. In all images, green represents cell membrane, Myr-Palm-GFP, and magenta represents nuclei, H2B-mCherry. Scale bars, 20 μm. N is the number of independent replicates.

fluorescence lifetime (Colom et al., 2018). After hypotonic shock, cell volume increased to reach a plateau about 15 min after the shock (Figure 4G). The fluorescence lifetime of FliptR—and thus tension—followed the same dynamics (Figure S4M). Notably, the volume change was due to an increase in cell height without changes in cell width (Figure 4H), as seen in rolls (Figures 2B and 2C), yet with a lower increase (Figure 2D). As expected, hyperosmotic shocks on flat epithelia caused an instantaneous lifetime decrease (Figure S4N) associated with a volume decrease of $\sim$50% with no recovery (Figures 4I and S4O). The global cell organization on flat mono-layers did not change, showing that volume change was again only accommodated through changes in cell height (Figure 4I). These results established that osmotic shocks could change cell volume and membrane tension in epithelia.

To test directly if osmosis was involved in the transient cell thickening after rolling, we intended to counteract this response by applying a concomitant hyperosmotic shock—the cells dramatically flattened (Figure 4J), preventing cell volume increase observed in isotonic conditions. These results supported the hypothesis that curvature-induced cell volume increase was due to changes in the osmotic balance.
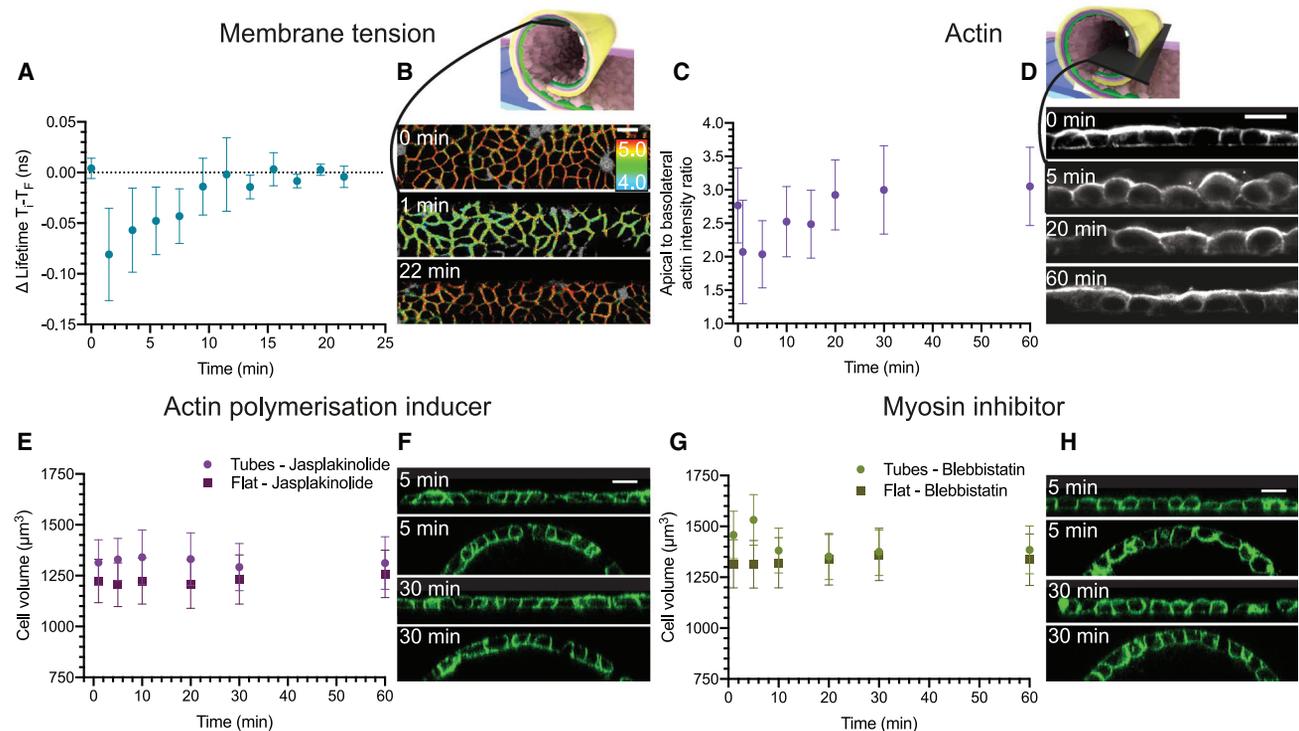
Figure 5. With ion channels, actin cytoskeleton and membrane tension control short and long-time scale response to curvature generation
(A) Mean values and SD of fluorescence lifetime (difference values of each time point [T_i] with the final time point [T_F]) on flat regions (0 min) and on tubes over time after cutting, n $\geq$ 4 images/time point, N = 4.
(B) Representative top views along the tubes (see diagram) at different time points after cutting. The color bar corresponds to lifetime in nanoseconds (ns).
(C) Mean values and SD of apical to basolateral actin intensity ratio on flat regions (0 min) and on tubes over time after cutting, n $\geq$ 31 images/time point, N $\geq$ 3.
(D) Representative orthogonal views along the tubes (see diagram) at different time points after cutting. Actin (SiR-Actin, gray).
(E–H) Weighted means and SEWM (with variance weights) of cell volume and representative orthogonal views on flat regions or tubes at 5 and 30 min after cutting of (E and F) jasplakinolide-treated cells on flat regions (dark violet squares) and on tubes (light violet circles) over time after cutting, n $\geq$ 14 images/time point, N = 3; and of (G and H) blebbistatin treatment on flat regions (dark green squares) and on tubes (green circles) over time after cutting, n $\geq$ 16 images/time point, N = 3. In (F) and (H), green represents cell membrane, Myr-Palm-GFP. Scale bars, 20 μm. N is the number of independent replicates.

To further test this hypothesis, we investigated membrane tension response to an epithelium rolling. Fluorescence lifetime instantaneously decreased upon rolling, earlier than the cell volume peak, and recovered to the initial value in about 10 min (Figures 5A and 5B) at the time when volume recovery was starting. Thus, tissue rolling correlated with a drop in membrane tension, followed by a volume increase that recovered once the tension was back to its initial value.

As volume changes of epithelial cells were mostly accommodated on the apical side, we wondered if the apical actin belt was maintained during cell shape change. Moreover, actin is a general regulator of membrane tension (Chugh et al., 2017), and its modulation could explain the rapid drop in tension and its recovery that we observed in cells upon rolling. Interestingly, the apical/basolateral actin fluorescence ratio quickly decreased after rolling (Figures 5C and 5D) due to a large decrease of apical actin staining, followed by a 20 min recovery.

We next wondered if actin depolymerization on the apical side was necessary to induce cell volume increase. When we used a jasplakinolide treatment to inhibit actin filament disassembly (Cramer, 1999), the cell volume slowly and partially increased before recovery (Figures 5E, 5F, and S5A). Thus, inhibition of actin belt depolymerization counteracted cell volume increase.

Conversely, when treated with blebbistatin, which disrupts myosin contractility, the dynamics of volume increase were similar to the non-treated condition (Figures 5G, 5H, and S5B). However, the resulting volume change was ~20% (instead of ~40%), probably because cells treated with blebbistatin had a higher initial volume. We then concluded that cell contractility had a minor role in the cell response to curvature change.

Then, we aimed to better understand the role of actin depolymerization in the cell swelling and membrane tension drop. First, we showed that actin depolymerized on rolls with the inverted sign of curvature (Figure S5C) but not in stretched epithelia as previously reported for even larger stretches (Harris et al., 2012; Figure S5D). In inverted rolls, the dynamics of actin depolymerization were the same as in the inward rolls (Figure 5C). In 15%-stretched and -compressed substrates, the actin apico-laterobasal intensity ratio remained constant, as observed for cell volume (Figure 2I).

We next quantified membrane tension dynamics in flat stretching experiments and showed that it remained unchanged (Figure S5E). These results suggested that whether actin depolymerized or not explains that tension and volume changed during rolling and not during stretching. To exclude any possible elastic compensation during stretching or compression because of
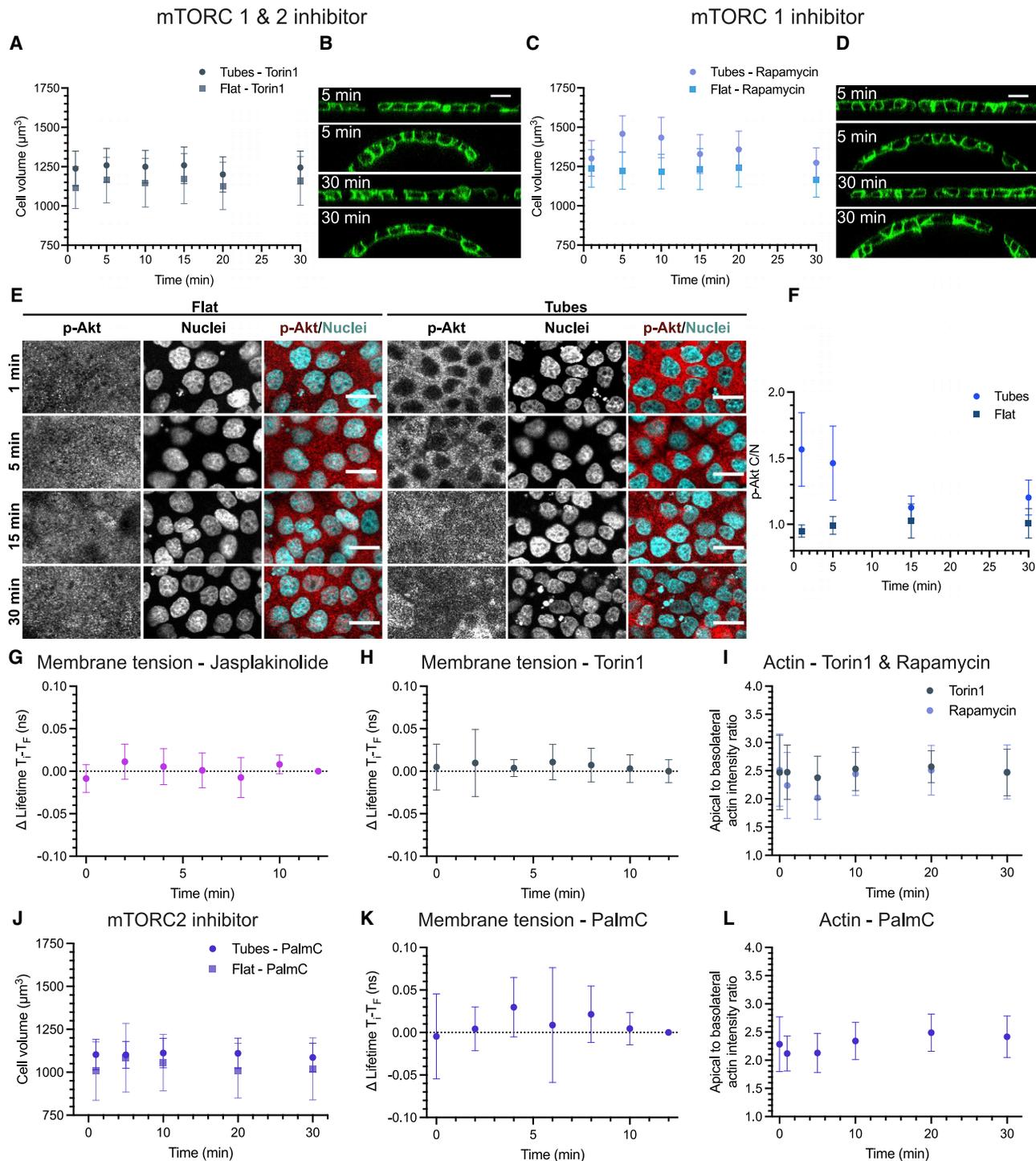
Figure 6. Short-time response involves mTORC2 activity and requires membrane tension drop

(A–D) Weighted means and SEWM (with variance weights) of cell volume and representative orthogonal views on flat regions or tubes at 5 and 30 min after cutting of (A and B) Torin1-treated cells on flat regions (gray squares) and on tubes (dark gray circles) over time after cutting, n ≥ 10 images/time point, N = 3; and of (C and D) rapamycin-treated cells on flat regions (dark blue squares) over time and on tubes (blue circles) over time after cutting, n ≥ 16 images/time point, N = 3.

(E) Representative images of cells fixed and stained for phosphorylated Akt (red) and nuclei (cyan) on flat regions close to the tubes over time and in tubes over time after cutting.

(F) Mean values and SD of the cytosolic/nuclear (C/N) fluorescent ratio of the phospho-Akt antibody at different time points after cutting on flat and tubes. n ≥ 8 images/time point, N = 1.

(legend continued on next page)

the rather small strain rate, we checked cell volume, actin polarization, and membrane tension on cell monolayers both compressed and stretched at a double rate of the maximal estimation of the PDMS compression upon rolling (Methods S3), i.e., 30% (Figures S5F–S5H). These experiments confirmed that no significant changes over time in cell volume, actin polarization, or membrane tension could be observed, even for high stretching and compression rates. Membrane tension increased moderately upon stretching and decreased very slowly during compression. The timescales at which the moderate changes of tension occurred support that they are not an immediate consequence of stretching and compression. Moreover, as cell volume and actin polymerization do not change in these experiments, they cannot cause these tension changes.

To test whether actin depolymerization alone would be sufficient to induce the membrane tension decrease and the subsequent volume increase during rolling, we depolymerized actin using latrunculin A. In epithelia grown on flat substrates, both cell volume and membrane tension did not show significant variations after latrunculin A treatment (Figures S6A and S6B), albeit we observed some small oscillations in the latter. In rolling experiments with pre-treated cells, latrunculin A inhibited the cell volume increase at 5 min after rolling (Figure S6C). This result supported the hypothesis of a collective response to curvature change, which requires tightly connected cells with an intact actin belt. In further support of this, latrunculin A treatment caused a gradual loss of cell-cell junctions and induced a moderate increase of cell volume after 30–40 min of total treatment. However, no E-cadherin reorganization was observed (Figure S6D) during rolling experiments, supporting the notion that cell-cell junction reorganization is not a part of the mechano-osmotic response of cells to curvature.

As actin, membrane tension, and osmotic response are critically dependent on the mammalian target of rapamycin complexes (mTORC) 1&2, we investigated their role in the response to curvature induction. We used Torin1 and rapamycin treatments to inhibit mTORC1&2 (Thoreen et al., 2009) and mTORC1, respectively (Roffay et al., 2021; Sehgal, 2003). In Torin1-treated cells, we observed a reduced volume increase (Figures 6A, 6B, and S6E) as compared with the rapamycin-treated cells (Figures 6C, 6D, and S6F). However, in both the cases, the volume peak was lower than in non-treated cells, and the recovery was delayed, suggesting that both cell volume increase and recovery involved both mTORC1 and mTORC2 signaling. In particular, these results suggested that the long-time response, i.e., cell volume recovery, mainly involved mTORC1, whereas the short-time response associated with cell swelling and membrane tension decrease mainly involved mTORC2. We further investigated mTORC2 activity *in situ* by employing a phospho-

specific antibody against Akt (Ser473), a residue directly phosphorylated by active mTORC2 (Figure 6E). We observed that the cytosolic/nuclear (C/N) fluorescent ratio of the phospho-Akt antibody increased upon rolling and gradually decreased (Figure 6F), with similar dynamics to membrane tension and actin depolymerization. This clearly shows a modification of Akt signaling within rolled cells. A reduction of the nuclear pool of phospho-Akt could be linked to a drop in mTORC2 activity associated with a drop in tension (Riggi et al., 2018; Roffay et al., 2021). However, how phospho-Akt shuttles between the nucleus and the cytoplasm, how it gets phosphorylated and dephosphorylated in the nucleus, and how the nuclear pool of phospho-Akt regulates down-stream targets are not fully understood (Martelli et al., 2012).

A membrane tension change upon rolling is required to induce cell volume change

To deepen our understanding of the interplay between actin and membrane tension dynamics during curvature-induced cell swelling, we compared drugs that interfered with actin or tension regulation and that mainly reduced cell volume increase. We observed that for both jasplakinolide- and Torin1-treated cells, both membrane tension (Figures 6G and 6H) and cell volume (Figures 5E and 6A) remained constant. Moreover, both actin depolymerization (Figure 6I) and cell volume (Figures 6A and 6C) increase appeared more significant in the rapamycin-treated cells compared with Torin1. These results suggested that mTORC2 is mainly involved in the curvature change adaptation. To confirm this hypothesis, we used palmitoyl-L-carnitine chloride (PalmC), which is known to inhibit TORC2 by reducing membrane tension (Riggi et al., 2018). We observed that on flat substrates, PalmC instantaneously induced a decrease in membrane tension (Figure S6G), while volume remained constant (Figure S6H). By rolling PalmC-treated cells, volume (Figures 6J and S6I) and membrane tension (Figure 6K) did not change, and actin only slightly depolymerized a few minutes after cutting (Figure 6L). In conclusion, mTORC2 plays an important role in the volume increase, which correlates with a membrane tension change upon rolling.

DISCUSSION

Altogether, our results showed that a flat epithelium curled into a tubular shape actively and instantaneously responded by depolymerizing apical actin and decreasing plasma membrane tension. This initial response was followed by a cell volume increase of ~40% 5 min after rolling and resulted from a swelling of the apical pole. Interestingly, this transient cell swelling was observed independently of the sign of rolling. Indeed, stretching

---

(G and H) Mean values and SD of fluorescence lifetime (difference values of each time point [T_i] with the final time point [T_F]) on flat regions (0 min) and on tubes over time after cutting of (G) jasplakinolide-treated cells, $n \geq 3$ images/time point, $N = 2$; and of (H) Torin1-treated cells, $n \geq 3$ images/time point, $N = 2$.

(I) Mean values and SD of apical to basolateral actin intensity ratio on flat regions (0 min) and on tubes of Torin1- and rapamycin-treated cells over time after cutting. $n \geq 15$ images/time point (Torin1), $n \geq 8$ images/time point (rapamycin), $N = 2$.

(J) Weighted means and SEWM (with variance weights) of cell volume after PalmC treatment on flat regions (light violet squares) and on tubes (dark violet circles) over time after cutting. $n \geq 5$ images/time point (flat), $n \geq 24$ images/time point (tubes), $N = 3$.

(K) Mean values and SD of fluorescence lifetime (difference values of each time point [T_i] with the final time point [T_F]) of PalmC-treated cells on flat regions (0 min) and on tubes over time after cutting. $n \geq 3$ images/time point, $N = 2$.

(L) Mean values and SD of apical to basolateral actin intensity ratio on flat regions (0 min) and on tubes of PalmC-treated cells over time after cutting, $n \geq 15$ images/time point, $N = 2$. N is the number of independent replicates. Scale bars, 20 μm.

or compressing cell monolayers did not induce any cell volume change. The main difference in the rolls is that bending cells are stretched on one side and compressed on the opposite side in the apico-basal axis.

When rolling, the entire field of constraints within the epithelium has to change, and resetting the force field to its initial value would require to entirely depolymerize the actin network. Indeed, when actin depolymerization is inhibited by a jasplakinolide treatment, or induced prior to rolling by latrunculin A, membrane tension decrease and cell volume increase do not occur, showing that the actin belt polymerization-depolymerization cycle is required for cell volume and membrane tension changes. Based on the observation that actin depolymerizes for both directions of epithelium rolling, we propose that this response allows resetting the contractile force field normally present in epithelia. On the reverse, in stretching-compression experiments, deformations occur in the cell plane, and force-field reorganization does not require actin depolymerization, as confirmed by the observations of constant actin signal and membrane tension. Then, the tension recovers while the volume peaks, supporting that the tension is re-equilibrated by cell swelling. Moreover, because volume increase happens a few minutes after tension decrease and mainly involves mTORC2 and ionic channels, we propose that the volume increase is an osmotic swelling to restore membrane tension in reaction to a stimulus perceived as a hypertonic shock.

In reaction to rolling, we observed a strong reduction of the phospho-Akt nuclear pool. In a general case, Akt being initially inactive in the cytoplasm, its activation—among other possibilities—occurs through phosphorylation by mTORC2 at the plasma membrane (Rosner et al., 2007). Phospho-Akt then translocates to the cytosol and the nucleus (Coa et al., 2019; Martelli et al., 2012). However, how the phosphorylation state regulates shuttling between the cytoplasm and the nucleus is still under debate (Martelli et al., 2012). In all cases, 1 min after rolling, the nuclear signal of phospho-Akt is already lower than at the equilibrium on flat regions. This observation is compatible with a rapid mTORC2 inactivation, but further investigations would be necessary to clearly decipher the correlation between the C/N ratio of phospho-Akt and mTORC2 activity. mTORC2 inactivation would be consistent with the fact that TORC2 activity is reduced by membrane tension loss (Riggi et al., 2018; Roffay et al., 2021), as tension drops immediately after rolling. Moreover, pre-inhibiting mTORC2 with Torin1 fully inhibits the cell volume increase after rolling (Figure 6A), supporting the notion that transient inactivation of mTORC2 may regulate cell volume increase.

Finally, the volume only fully recovers when apical actin is fully repolymerized, supporting the idea that actin at least partially drives cell volume equilibrium. Interestingly, cell swelling is only seen in large-scale curvature induction, over curved distances of hundreds of microns, supporting the notion that only a collective reaction of cells to curvature can trigger this volume increase at the level of every single cell.

Overall, we showed that epithelium is a unique active material that transiently swells upon rolling. Indeed, usual materials either reduce their volume or keep it upon bending or other curvature-inducing deformations. From a physiological point of view, these results may also bring new insights into the mechanisms of adaptation of very dynamic epithelia, such as lung alveoli, whose curvature regularly changes during the breathing cycle in a timescale of few seconds, intestinal villi, acini, and blood vessels.

These results suggested that the reason for such effect would be to participate in the necessary physiological adaptation of polarized epithelial cells to the large deformation produced by the new curvature—only a compact epithelium induces the cell swelling upon rolling, and the organization of E-cadherins, known to be involved in tissue mechanosensing (Yang et al., 2022), is maintained during tissue deformation, suggesting that it guarantees the collective cell sensing to the global shape change. Moreover, the depolymerization of apical actin seems necessary to adapt the shape and the forces in the actin belt of each cell. The resulting drop in tension would cause the cell to swell, as observed in mitotic cells (Son et al., 2015; Zlotek-Zlotkiewicz et al., 2015), inducing the repolymerization of actin to recover volume (Sedzinski et al., 2011). Finally, the reformation of the actin belt will be adapted to the new curvature, recovering the force field that maintains epithelial cell cohesiveness. In this scenario, the active cell swelling is required so that cells do not lose volume and change shape too dramatically while the actin belt is disassembled. Thus, tissue remodeling requires a complex interplay between ion transportation, actin organization, and volume regulation—possibly orchestrated by TORCs signaling (Demian et al., 2019)—to adapt single-cell mechanics to the new shape of the tissue.

In conclusion, our work shows that a rapid shape change induces transient cell volume increase via a mechano-osmotic balance of the cell volume with membrane tension and actin forces. Indeed, it was theoretically (Jiang and Sun, 2013) predicted and experimentally (Guo et al., 2017) shown that external properties, such as indentation forces, substrate stiffness, or limited spreading area, and thus cell shape changes, can induce active cell volume changes due to water and ion channel activation. In single cells, it has been recently shown that when tension increases, the volume drops, and, interestingly, this response is inverse to the one we observed and still occurs with transient dynamics as observed in this study. This behavior is explained by a mechano-osmotic coupling—which involves actin cortex, ion fluxes, and membrane tension—and with the timescale of cell shape deformation that is inversely proportional to the amplitude of volume change (Venkova et al., 2022). This is consistent with our observation of a peak of cell volume increase following a rapid bending of less than 10 s. It is also consistent with the fact that a slow membrane tension decrease in PalmC-treated cells did not change the cell volume. Finally, the absence of cell swelling upon rolling and on flat substrates with latrunculin A-treated cells showed that actin depolymerization alone is necessary but not sufficient to induce volume change. Further investigations would be necessary to precisely describe the causal relationship between actin depolymerization, ion fluxes, and membrane tension, which, however, are strongly interconnected and therefore difficult to disrupt independently.

Limitations of the study

We reported cell response to a rapid curvature induction in both directions, with a robust technique that produces inward and outward deformations of an initially flat cell monolayer. However, this approach is not reversible, and the duration of the deformation is fixed to a few seconds. We also deformed flat monolayers

in wavy shapes, alternating both signs of curvature. In this case, the amplitude and the time of the deformation can be modulated, but the range of the geometrical parameters is quite limited, and curvature induction is also associated with a small compression. By improving these approaches, it will be possible to have access to a larger panel of *in vivo* movements occurring during embryogenesis and organ activity. Although we showed a clear involvement of actin polymerization, cell membrane tension, cell volume, and mTORC2 activity in the adaptation to curvature, further studies will be necessary to deeply investigate their causal relationship and their effect on cell physiology. We highlighted an active cell response, very specific to a persistent curvature change, which also demonstrated a complex mechano-osmotic coupling behind cell volume regulation that couples single-cell response to large-scale tissue deformation. A larger application of this approach to other cell types will establish the universality of the results obtained in this study with MDCK cells.

STAR★METHODS

Detailed methods are provided in the online version of this paper and include the following:

- KEY RESOURCES TABLE
- RESOURCE AVAILABILITY
  - Lead contact
  - Materials availability
  - Data and code availability
- EXPERIMENTAL MODEL AND SUBJECT DETAILS
  - Cell lines
- METHOD DETAILS
  - Curvature-inducible substrate preparation
  - Cell culture and sample preparation
  - Drug treatments
  - Fluorescence labelling
  - Imaging
- QUANTIFICATION AND STATISTICAL ANALYSIS
  - Segmentation and cell volume quantification
  - Actin intensity quantification
  - p-Akt intensity quantification
  - Curvature quantification of PDMS tubes and wavy substrates
  - Fluorescence lifetime analysis

SUPPLEMENTAL INFORMATION

Supplemental information can be found online at https://doi.org/10.1016/j.devcel.2022.04.017.

REFERENCES

Bade, N.D., Xu, T., Kamien, R.D., Assoian, R.K., and Stebe, K.J. (2018). Gaussian curvature directs stress fiber orientation and cell migration. Biophys. J. *114*, 1467–1476.

Baptista, D., Teixeira, L., van Blitterswijk, C., Giselbrecht, S., and Truckenmüller, R. (2019). Overlooked? Underestimated? Effects of substrate curvature on cell behavior. Trends Biotechnol *37*, 838–854.

Baughman, R.H., Stafström, S., Cui, C., and Dantas, S.O. (1998). Materials with negative compressibilities in one or more dimensions. Science *279*, 1522–1524.

Bidan, C.M., Fratzl, M., Coullomb, A., Moreau, P., Lombard, A.H., Wang, I., Balland, M., Boudou, T., Dempsey, N.M., Devillers, T., et al. (2018). Magneto-active substrates for local mechanical stimulation of living cells. Sci. Rep. *8*, 1464.

Blonski, S., Aureille, J., Badawi, S., Zaremba, D., Pernet, L., Grichine, A., Fraboulet, S., Korczyk, P.M., Recho, P., Guilluy, C., et al. (2021). Direction of epithelial folding defines impact of mechanical forces on epithelial state. Dev. Cell *56*, 3222–3234.e6.

Broaders, K.E., Cerchiari, A.E., and Gartner, Z.J. (2015). Coupling between apical tension and basal adhesion allow epithelia to collectively sense and respond to substrate topography over long distances. Integr. Biol. *7*, 1611–1621.

Brunette, D.M. (1984). Mechanical stretching increases the number of epithelial cells synthesizing DNA in culture. J. Cell Sci. *69*, 35–45.

Burke, R.D., Myers, R.L., Sexton, T.L., and Jackson, C. (1991). Cell movements during the initial phase of gastrulation in the Sea Urchin Embryo. Dev. Biol. *146*, 542–557.

Callens, S.J.P., Uyttendaele, R.J.C., Fratila-Apachitei, L.E., and Zadpoor, A.A. (2020). Substrate curvature as a cue to guide spatiotemporal cell and tissue organization. Biomaterials *232*, 119739.

Cheng, X., and Zhang, Y. (2019). Micro/nanoscale 3D assembly by rolling, folding, curving, and buckling approaches. Adv. Mater. *31*, e1901895.

Chin, A.M., Hill, D.R., Aurora, M., and Spence, J.R. (2017). Morphogenesis and maturation of the embryonic and postnatal intestine. Semin. Cell Dev. Biol. *66*, 81–93.

Chugh, P., Clark, A.G., Smith, M.B., Cassani, D.A.D., Dierkes, K., Ragab, A., Roux, P.P., Charras, G., Salbreux, G., and Paluch, E.K. (2017). Actin cortex architecture regulates cell surface tension. Nat. Cell Biol. *19*, 689–697.

Coa, L.L., Abreu, T.F., Tashima, A.K., Green, J., Pascon, R.C., Vallim, M.A., and Machado, J. (2019). AKT/protein kinase B associates with β-actin in the nucleus of melanoma cells. Biosci. Rep. *39*, 1–15.

Colom, A., Derivery, E., Soleimanpour, S., Tomba, C., Molin, M.D., Sakai, N., González-Gaitán, M., Matile, S., and Roux, A. (2018). A fluorescent membrane tension probe. Nat. Chem. *10*, 1118–1125.

Cramer, L.P. (1999). Role of actin-filament disassembly in lamellipodium protrusion in motile cells revealed using the drug jasplakinolide. Curr. Biol. *9*, 1095–1105.

Dal Molin, M., Verolet, Q., Colom, A., Letrun, R., Derivery, E., Gonzalez-Gaitan, M., Vauthey, E., Roux, A., Sakai, N., and Matile, S. (2015). Fluorescent flippers for mechanosensitive membrane probes. J. Am. Chem. Soc. *137*, 568–571.

Decher, N., Lang, H.J., Nilius, B., Brüggemann, A., Busch, A.E., and Steinmeyer, K. (2001). DCPIB is a novel selective blocker of ICl,swell and prevents swelling-induced shortening of guinea-pig atrial action potential duration. Br. J. Pharmacol. *134*, 1467–1479.

Delarue, M., Brittingham, G.P., Pfeffer, S., Surovtsev, I.V., Pinglay, S., Kennedy, K.J., Schaffer, M., Gutierrez, J.I., Sang, D., Poterewicz, G., et al. (2018). mTORC1 controls phase separation and the biophysical properties of the cytoplasm by tuning crowding. Cell *174*, 338–349.e20.

Demian, W.L., Persaud, A., Jiang, C., Coyaud, É., Liu, S., Kapus, A., Kafri, R., Raught, B., and Rotin, D. (2019). The ion transporter NKCC1 links cell volume to cell mass regulation by suppressing mTORC1. Cell Rep *27*, 1886–1896.e6.

Duda, M., Kirkland, N.J., Khalilgharibi, N., Tozluoglu, M., Yuen, A.C., Carpi, N., Bove, A., Piel, M., Charras, G., Baum, B., et al. (2019). Polarization of myosin II refines tissue material properties to buffer mechanical stress. Dev. Cell *48*, 245–260.e7.

Egunov, A.I., Inaba, A., Gree, S., Malval, J.P., Tamura, K., Saito, Y., and Luchnikov, V.A. (2016a). Time-programmed release of fluoroscein isocyanate dextran from micro-pattern-designed polymer scrolls. J. Control. Release *233*, 39–47.

Egunov, A.I., Korvink, J.G., and Luchnikov, V.A. (2016b). Polydimethylsiloxane bilayer films with an embedded spontaneous curvature. Soft Matter *12*, 45–52.

Eisenhoffer, G.T., Loftus, P.D., Yoshigi, M., Otsuna, H., Chien, C.-B., Morcos, P.A., and Rosenblatt, J. (2012). Crowding induces live cell extrusion to maintain homeostatic cell numbers in epithelia. Nature *484*, 546–549.

Eltschinger, S., and Loewith, R. (2016). TOR complexes and the maintenance of cellular homeostasis. Trends Cell Biol *26*, 148–159.

Feiner, R., Engel, L., Fleischer, S., Malki, M., Gal, I., Shapira, A., Shacham-Diamand, Y., and Dvir, T. (2016). Engineered hybrid cardiac patches with multifunctional electronics for online monitoring and regulation of tissue function. Nat. Mater. *15*, 679–685.

Gatt, R., and Grima, J.N. (2008). Negative compressibility. Phys. Stat. Sol. (RRL) *2*, 236–238.

Gérémie, L., Ilker, E., Bernheim-Dennery, M., Cavaniol, C., Viovy, J.-L., Vignjevic, D.M., Joanny, J.-F., and Descroix, S. (2022). Evolution of a confluent gut epithelium under on-chip cyclic stretching. Phys. Rev. Res. *4*, 1–15.

Gladman, A.S., Matsumoto, E.A., Nuzzo, R.G., Mahadevan, L., and Lewis, J.A. (2016). Biomimetic 4D printing. Nat. Mater. *15*, 413–418.

Gudipaty, S.A., Lindblom, J., Loftus, P.D., Redd, M.J., Edes, K., Davey, C.F., Krishnegowda, V., and Rosenblatt, J. (2017). Mechanical stretch triggers rapid epithelial cell division through Piezo1. Nature *543*, 118–121.

Guo, M., Pegoraro, A.F., Mao, A., Zhou, E.H., Arany, P.R., Han, Y., Burnette, D.T., Jensen, M.H., Kasza, K.E., Moore, J.R., et al. (2017). Cell volume change through water efflux impacts cell stiffness and stem cell fate. Proc. Natl. Acad. Sci. USA *114*, E8618–E8627.

Harris, A.R., Peter, L., Bellis, J., Baum, B., Kabla, A.J., and Charras, G.T. (2012). Characterizing the mechanics of cultured cell monolayers. Proc. Natl. Acad. Sci. USA *109*, 16449–16454.

Hoffmann, E.K., Lambert, I.H., and Pedersen, S.F. (2009). Physiology of cell volume regulation in vertebrates. Physiol. Rev. *89*, 193–277.

Hong, L., DuMond, M., Zhu, M., Tsugawa, S., Li, C.-B., Boudaoud, A., Hamant, O., and Roeder, A.H.K. (2018). Heterogeneity and robustness in plant morphogenesis: From cells to organs. Annu. Rev. Plant Biol. *69*, 469–495.

Ionov, L. (2018). 4D biofabrication: materials, methods, and applications. Adv. Healthc. Mater. *7*, e1800412.

Jamal, M., Kadam, S.S., Xiao, R., Jivan, F., Onn, T.M., Fernandes, R., Nguyen, T.D., and Gracias, D.H. (2013). Bio-origami hydrogel scaffolds composed of photocrosslinked PEG bilayers. Adv. Healthc. Mater. *2*, 1142–1150.

Jentsch, T.J. (2016). VRACs and other ion channels and transporters in the regulation of cell volume and beyond. Nat. Rev. Mol. Cell Biol. *17*, 293–307.

Jiang, H., and Sun, S.X. (2013). Cellular pressure and volume regulation and implications for cell mechanics. Biophys. J. *105*, 609–619.

Kim, H.Y., Varner, V.D., and Nelson, C.M. (2013). Apical constriction initiates new bud formation during monopodial branching of the embryonic chicken lung. Development *140*, 3146–3155.

Kotyk, T., Dey, N., Ashour, A.S., Balas-Timar, D., Chakraborty, S., Ashour, A.S., and Tavares, J.M.R.S. (2016). Measurement of glomerulus diameter and Bowman's space width of renal albino rats. Comput. Methods Programs Biomed *126*, 143–153.

Kumar, K., Nandan, B., Luchnikov, V., Gowd, E.B., and Stamm, M. (2009). Fabrication of metallic microtubes using self-rolled polymer tubes as templates. Langmuir *25*, 7667–7674.

Lakes, R., and Wojciechowski, K.W. (2008). Negative compressibility, negative Poisson's ratio, and stability. Phys. Status Solidi Basic Res. *245*, 545–551.

Lecuit, T., and Lenne, P.-F. (2007). Cell surface mechanics and the control of cell shape, tissue patterns and morphogenesis. Nat. Rev. Mol. Cell Biol. *8*, 633–644.

Luchnikov, V., Lonov, L., and Stamm, M. (2011). Self-rolled polymer tubes: novel tools for microfluidics, microbiology, and drug-delivery systems. Macromol. Rapid Commun. *32*, 1943–1952.

Machado, S., Mercier, V., and Chiaruttini, N. (2019). LimeSeg: a coarse-grained lipid membrane simulation for 3D image segmentation. BMC Bioinformatics *20*, 2.

Maechler, F.A., Allier, C., Roux, A., and Tomba, C. (2019). Curvature-dependent constraints drive remodeling of epithelia. J. Cell Sci. *132*. jcs222372.

Martelli, A.M., Tabellini, G., Bressanin, D., Ognibene, A., Goto, K., Cocco, L., and Evangelisti, C. (2012). The emerging multiple roles of nuclear Akt. Biochim. Biophys. Acta *1823*, 2168–2178.

Martin, A.C., and Goldstein, B. (2014). Apical constriction: themes and variations on a cellular mechanism driving morphogenesis. Development *141*, 1987–1998.

Mei, Y., Huang, G., Solovev, A.A., Ureña, E.B., Mönch, I., Ding, F., Reindl, T., Fu, R.K.Y., Chu, P.K., and Schmidt, O.G. (2008). Versatile approach for integrative and functionalized tubes by strain engineering of nanomembranes on polymers. Adv. Mater. *20*, 4085–4090.

Pieuchot, L., Marteau, J., Guignandon, A., Dos Santos, T., Brigaud, I., Chauvy, P.F., Cloatre, T., Ponche, A., Petithory, T., Rougerie, P., et al. (2018). Curvotaxis directs cell migration through cell-scale curvature landscapes. Nat. Commun. *9*, 3995.

Rauzi, M., Hočevar Brezavšček, A., Ziherl, P., and Leptin, M. (2013). Physical models of mesoderm invagination in *Drosophila* embryo. Biophys. J. *105*, 3–10.

Riggi, M., Niewola-Staszkowska, K., Chiaruttini, N., Colom, A., Kusmider, B., Mercier, V., Soleimanpour, S., Stahl, M., Matile, S., Roux, A., et al. (2018). Decrease in plasma membrane tension triggers PtdIns(4,5)P2 phase separation to inactivate TORC2. Nat. Cell Biol. *20*, 1043–1051.

Roffay, C., Molinard, G., Kim, K., Urbanska, M., Andrade, V., Barbarasa, V., Nowak, P., Mercier, V., García-Calvo, J., Matile, S., et al. (2021). Passive coupling of membrane tension and cell volume during active response of cells to osmosis. Proc. Natl. Acad. Sci. USA *118*.

Rosner, M., Hanneder, M., Freilinger, A., and Hengstschläger, M. (2007). Nuclear/cytoplasmic localization of Akt activity in the cell cycle. Amino Acids *32*, 341–345.

Sankar, K.D., Bhanu, P.S., Ramalingam, K., Kiran, S., and Ramakrishna, B.A. (2013). Histomorphological and morphometrical changes of placental terminal villi of normotensive and preeclamptic mothers. Anat. Cell Biol. *46*, 285–290.

Sawyer, J.M., Harrell, J.R., Shemer, G., Sullivan-Brown, J., Roh-Johnson, M., and Goldstein, B. (2010). Apical constriction: a cell shape change that can drive morphogenesis. Dev. Biol. *341*, 5–19.

Schindelin, J., Arganda-Carreras, I., Frise, E., Kaynig, V., Longair, M., Pietzsch, T., Preibisch, S., Rueden, C., Saalfeld, S., and Schmid, B. (1990). Fiji: An open-source platform for biological-image analysis. Nat. Methods 9, 676–682.

Schoenwolf, G.C., and Smith, J.L. (1990). Mechanisms of neurulation: traditional viewpoint and recent advances. Development 109, 243–270.

Sedzinski, J., Biro, M., Oswald, A., Tinevez, J.Y., Salbreux, G., and Paluch, E. (2011). Polar actomyosin contractility destabilizes the position of the cytokinetic furrow. Nature 476, 462–466.

Sehgal, S.N. (2003). Sirolimus: its discovery, biological properties, and mechanism of action. Transplant. Proc. 35, 7S–14S.

Shyer, A.E., Tallinen, T., Nerurkar, N.L., Wei, Z., Gil, E.S., Kaplan, D.L., Tabin, C.J., and Mahadevan, L. (2013). Villification: how the gut gets its villi. Science 342, 212–218.

Son, S., Kang, J.H., Oh, S., Kirschner, M.W., Mitchison, T.J., and Manalis, S. (2015). Resonant microchannel volume and mass measurements show that suspended cells swell during mitosis. J. Cell Biol. 211, 757–763.

Streichan, S.J., Hoerner, C.R., Schneidt, T., Holzer, D., and Hufnagel, L. (2014). Spatial constraints control cell proliferation in tissues. Proc. Natl. Acad. Sci. USA 111, 5586–5591.

Sweeton, D., Parks, S., Costa, M., and Wieschaus, E. (1991). Gastrulation in Drosophila: the formation of the ventral furrow and posterior midgut invaginations. Development 112, 775–789.

Teshima, T.F., Nakashima, H., Ueno, Y., Sasaki, S., Henderson, C.S., and Tsukada, S. (2017). Cell assembly in self-foldable multi-layered soft micro-rolls. Sci. Rep. 7, 17376.

Thoreen, C.C., Kang, S.A., Chang, J.W., Liu, Q., Zhang, J., Gao, Y., Reichling, L.J., Sim, T., Sabatini, D.M., and Gray, N.S. (2009). An ATP-competitive mammalian target of rapamycin inhibitor reveals rapamycin-resistant functions of mTORC1. J. Biol. Chem. 284, 8023–8032.

Tomba, C., Petithory, T., Pedron, R., Airoudj, A., Di Meglio, I., Roux, A., and Luchnikov, V. (2019). Laser-assisted strain engineering of thin elastomer films to form variable wavy substrates for cell culture. Small 15, e1900162.

Tozluoğlu, M., Duda, M., Kirkland, N.J., Barrientos, R., Burden, J.J., Muñoz, J.J., and Mao, Y. (2019). Planar differential growth rates initiate precise fold positions in complex epithelia. Dev. Cell 51, 299–312.e4.

Trushko, A., Di Meglio, I., Merzouki, A., Blanch-Mercader, C., Abuhattum, S., Guck, J., Alessandri, K., Nassoy, P., Kruse, K., Chopard, B., et al. (2020).

Buckling of an epithelium growing under spherical confinement. Dev. Cell 54, 655–668.e6.

Vallés, P.G., Bocanegra, V., Gil Lorenzo, A., and Costantino, V.V. (2015). Physiological functions and regulation of the Na+/H+ exchanger [NHE1] in renal tubule epithelial cells. Kidney Blood Press. Res. 40, 452–466.

Venkova, L., Vishen, A.S., Lembo, S., Srivastava, N., Duchamp, B., Ruppel, A., Williart, A., Vassilopoulos, S., Deslys, A., Garcia Arcos, J.M.G., et al. (2022). A mechano-osmotic feedback couples cell volume to the rate of cell deformation. Elife 11, e72381.

Werner, M., Blanquer, S.B.G., Haimi, S.P., Korus, G., Dunlop, J.W.C., Duda, G.N., Grijpma, D.W., and Petersen, A. (2017). Surface curvature differentially regulates stem cell migration and differentiation via altered attachment morphology and nuclear deformation. Adv. Sci. 4, 1600347.

Wyatt, T.P.J., Fouchard, J., Lisica, A., Khalilgharibi, N., Baum, B., Recho, P., Kabla, A.J., and Charras, G.T. (2020). Actomyosin controls planarity and folding of epithelia in response to compression. Nat. Mater. 19, 109–117.

Xi, W., Sonam, S., Beng Saw, T., Ladoux, B., and Teck Lim, C. (2017). Emergent patterns of collective cell migration under tubular confinement. Nat. Commun. 8, 1517.

Yablonskiy, D.A., Sukstanskii, A.L., Leawoods, J.C., Gierada, D.S., Bretthorst, G.L., Lefrak, S.S., Cooper, J.D., and Conradi, M.S. (2002). Quantitative in vivo assessment of lung microstructure at the alveolar level with hyperpolarized 3He diffusion MRI. Proc. Natl. Acad. Sci. USA 99, 3111–3116.

Yamashita, T., Kollmannsberger, P., Mawatari, K., Kitamori, T., and Vogel, V. (2016). Cell sheet mechanics : how geometrical constraints induce the detachment of cell sheets from concave surfaces. Acta Biomater 45, 85–97.

Yang, Y.A., Nguyen, E., Sankara Narayana, G.H.N.S., Heuzé, M., Fu, C., Yu, H., Mège, R.M., Ladoux, B., and Sheetz, M.P. (2022). Local contractions regulate E-cadherin rigidity sensing. Sci. Adv. 8, eabk0387.

Yevick, H.G., Duclos, G., Bonnet, I., and Silberzan, P. (2015). Architecture and migration of an epithelium on a cylindrical wire. Proc. Natl. Acad. Sci. USA 112, 5944–5949.

Yuan, B., Jin, Y., Sun, Y., Wang, D., Sun, J., Wang, Z., Zhang, W., and Jiang, X. (2012). A strategy for depositing different types of cells in three dimensions to mimic tubular structures in tissues. Adv. Mater. 24, 890–896.

Zlotek-Zlotkiewicz, E., Monnier, S., Cappello, G., Le Berre, M., and Piel, M. (2015). Optical volume and mass measurements show that mammalian cells swell during mitosis. J. Cell Biol. 211, 765–774.

STAR★METHODS

KEY RESOURCES TABLE

REAGENT or RESOURCE	SOURCE	IDENTIFIER
Antibodies		
Mouse anti-Ezrin	BD Biosciences	Cat# 610602; RRID: AB_397940
Rabbit anti-phospho-Akt (Ser473) or p-Akt	Cell Signaling Technology	Cat# 4060
Donkey anti-mouse, Alexa Fluor 488	Invitrogen	Cat# A21202; RRID: AB_141607
Donkey anti-rabbit, Alexa Fluor 488	Invitrogen	Cat# A21206; RRID: AB_2535792
Chemicals, peptides, and recombinant proteins		
Polydimethylsiloxane (PDMS)	Dow Corning	Sylgard 184 silicone elastomer kit
Fish gelatin	Sigma Aldrich	Cat# G7041
Toluene	Fisher Chemical	Cat# T/2300/15
Silicon oil	VWR	Cat# 47 V 350
Isopropanol	Fisher Chemical	Cat# P/7500/15
Fibronectin	Gibco	Cat# 33016015
Phosphate-buffered saline (PBS)	Gibco	Cat# 18912014
DMEM, high glucose, GlutaMAX™ Supplement, no sodium pyruvate	Gibco	Cat# 61965026
Fetal Bovine Serum (FBS)	Gibco	Cat# 10270106, Lot# 41G1840K
Penicillin-Streptomycin (PS)	Gibco	Cat# 15140122
MEM Non-Essential Amino Acids (NEAA)	Gibco	Cat# 11140035
Trypsin TrypLE express	Gibco	Cat# 12605010
Formaldehyde solution (PFA)	Sigma-Aldrich	Cat# F8775
Sucrose	PanReac AppliChem ITW Reagents	Cat# A2211
Leibovitz's L15 medium, no phenol red	Gibco	Cat# 21083027
DCPIB	Tocris	Cat# 1540
EIPA	Tocris	Cat# 3378
Bumetanide	Sigma-Aldrich	Cat# B3023
Furosemide	Sigma-Aldrich	Cat# F4381
Jasplakinolide	Enzo Life Sciences	Cat# ALX-350-275
Blebbistatin	Sigma-Aldrich	Cat# B0560
Torin1	LC Laboratories	Cat# T-7887
Rapamycin	LC Laboratories	Cat# R-5000
Dymethyl sulfoxide (DMSO)	Sigma-Aldrich	Cat# D2650
Latrunculin A	Sigma-Aldrich	Cat# L5163
Palmitoyl-L-carnitine chloride (PalmC)	Sigma-Aldrich	Cat# P4509
CellMask Deep Red Plasma Membrane Dye	Invitrogen	Cat# C10046
Hoechst 33342	Invitrogen	Cat# H3570
SiR-Actin	Spirochrome	Cat# SC001
Saponin	Axonlab	Cat# A4518,0100
Sodium pyrophosphate tetrabasic decahydrate NaPPi	Sigma-Aldrich	Cat# S9515
Sodium fluorite NaF	Honeywell Fluka	Cat# 71522
b-glycerophosphate disodium salt hydrate	Sigma-Aldrich	Cat# G9891
4-Nitrophenyl phosphate disodium salt hexahydrate pNPP	PanReac AppliChem ITW Reagents	Cat# A1442.0005
Flipper-TR	Spirochrome	Cat# SC020

(Continued on next page)

Continued

REAGENT or RESOURCE	SOURCE	IDENTIFIER
Fluorescein dextran, av. mol. wt. 40,000	Sigma-Aldrich	Cat# FD40S
Triton x100	PanReac AppliChem ITW Reagents	Cat# A1388
Bovine Serum Albumin (BSA)	PanReac AppliChem ITW Reagents	Cat# A1391
Deposited data		
Raw and analyzed data	Mendeley Data	https://doi.org/10.17632/9v9xfms555.1
Experimental models: Cell lines		
Madin-Darby Canin Kidney II (MDCK-II)	ECACC	Cat# 00062107
MDCKII Myr-PALM-GFP H2B-mCherry	(Tomba et al., 2019)	N/A
MDCK E-cadherin-GFP	A gift from the lab of D. J. Müller (ETH Zurich, Basel, Switzerland)	N/A
Software and algorithms		
Zen 2012	Carl Zeiss	N/A
Imaris 8.4.2	Oxford Instruments	N/A
SlideBook 6	3i (Intelligent Imaging Innovations)	N/A
LimeSeg	https://imagej.net/plugins/limeseg	(Machado et al., 2019)
Fiji	https://imagej.net/software/fiji/	(Schindelin et al., 2012)
LAS-X 2021	Leica	N/A
NIS-Elements	Nikon	N/A
SymPhoTime 64	PicoQuant	N/A
Icy 1.0	https://icy.bioimageanalysis.org/	N/A
Prism 9	GraphPad	N/A
Illustrator CS6	Adobe	N/A
Blender 2.79	https://www.blender.org/	N/A
Other		
Glass microscope slides	VWR	Cat# 631-1550
Plasma cleaner	Harrick Plasma	PDC-32G
Spin coater	SPS	Cat# Spin150
Silicone elastomer films	Silex Ltd	Cat# HT6240 40SH
Laser beam	Gravotech	Cat# LS100
Glass-bottom dishes	MatTek	Cat# P35G-1.5-20-C
Upright microscope LSM710	Carl Zeiss	N/A
Objective Plan-Apochromat 20x/1.0 N.A. DIC M27 75mm	Carl Zeiss	Cat# 421452-9800-000
Inverted microscope Nikon Eclipse Ti A1R	Nikon	N/A
Pulsed 485nm laser	PicoQuant	Cat# LDH-D-C-485
Objective Apo LWD 40X/1.15 N.A. WI	Nikon	N/A
Objective Plan Apo Lambda 100X/1.45 N.A.	Nikon	N/A
Upright microscope Leica SP8 LIVE FALCON	Leica	N/A
Objective HC FLUOTAR 25X/0.95 N.A.	Leica	Cat# 11506375
CO_2 and humidity controller	Okolab	OKO-Touch
Inverted microscope Nikon Eclipse Ti	Nikon	N/A
Objective 60X Apochromat TIRF /1.49 N.A. DIC	Nikon	N/A
Osmometer	Löser	Type 15

RESOURCE AVAILABILITY

Lead contact
Further information and requests for resources and reagents should be directed to and will be fulfilled by the lead contact, Aurélien Roux (aurelien.roux@unige.ch).

Materials availability
This study did not generate new unique reagents. There are no restrictions on any data or materials presented in this paper.

Data and code availability
- The raw data related to each figure have been deposited at Mendeley data (https://doi.org/10.17632/9v9xfms555.1).
- This paper does not report original code.
- Any additional information required to reanalyze the data reported in this paper is available from the lead contact upon request.

EXPERIMENTAL MODEL AND SUBJECT DETAILS

Cell lines
Madin Darby canine kidney II (MDCK-II) cells were purchased from ECACC, MDCK Myr-Palm-GFP H2B-mCherry cell line stably expressing the nucleus marker H2B-RFP and the plasma membrane marker Myr-Lyn-GFP was generated as previously described (Tomba et al., 2019), and MDCK E-cadherin-GFP cells were a kind gift of D. J. Müller (ETH Zurich, Basel). Cell lines were regularly tested negative for contamination with mycoplasma (Eurofins GATC Biotech, Germany).

METHOD DETAILS

Curvature-inducible substrate preparation
Self-rolling substrates with concave curvature
Ethanol-washed glass microscope slides (1 mm thick) were diamond-cut to a size of 15x25 mm. Then, ∼150 μl of Polydimethylsiloxane (PDMS, 10 wt% of curing agent) was poured on each piece of glass slide, vacuum-degassed for 10min, and cured at 100°C for 15 min. This PDMS layer serves to obtain a sharp cut of material above it, allowing the blade to lean on it. The PDMS surface was then activated using a plasma cleaner for 45 s, though a 0.5 cm high PDMS mask with a central hole of 0.5 cm by 2 cm. ∼200 μl of a 3% wt/vol of fish gelatin water solution were incubated >4 h on the activated surface. Then, ∼200 μl of a solution of PDMS Sylgard 184, curing agent and Toluene mixed in a 10:1:10 proportion were spin-coated onto the gelatin/PDMS surface (600 rpm/s, 3000 rpm, 50s), and reticulated on a hotplate at 110°C for 30 min. Then, ∼200 μl of a second solution of PDMS Sylgard 184, curing agent, silicon oil and Toluene mixed in a 5:5:0.5:10 proportion were spin-coated (600 rpm/s and, 1500 rpm, 50 s), and reticulated as before. The substrate was finally incubated in isopropanol overnight to extract the silicon oil. Then, on the day of cell seeding, the central part of the surface was plasma activated for 45s, through a 0.5 cm thick PDMS mask with a central window of 0.5 x 2cm^2. Then, the activated surface was incubated with fibronectin (1.8 μg cm^{-2}) in phosphate-buffered saline (PBS 1 h) to allow for cell adhesion.
Self-rolling substrates with convex curvature
The fabrication steps were the same than above, but the order of the two last layers was inverted, with spin-coating of the silicon oil-free PDMS solution being the last step.
Wavy substrates
As previously described (Tomba et al., 2019), silicone elastomer films (super clear sheet, 0.5 mm thick) were prestressed up to 100% of its length with homemade stretchers (composition: stainless steel and Teflon) and exposed with a laser beam. The same stretchers were used for the experiments of compression and stretching of a flat cell monolayer.

Cell culture and sample preparation
Madin Darby canine kidney II (MDCK-II), MDCK Myr-Palm-GFP H2B-mCherry and MDCK E-cadherin-GFP cells were cultured in DMEM supplemented with 10% fetal bovine serum (FBS), 1% Penicillin-Streptomycin (PS) and 1% non essential amino acids (NEAA), at 37°C and 5% CO$_2$.

After trypsinization, cells were seeded onto the fibronectin-coated of the substrate at 0.6 10^6 cells cm^{-2} (or 0.3 10^6 cells cm^{-2} when indicated) and let for adhesion in the incubator for ∼4 h. Then, the medium was gently removed and samples were submerged of fresh warm medium. After ∼20 h, non-adherent cells were gently flushed away using a 1 ml pipette tip. Samples were further processed as following.
Cells on self-rolling substrates
By cutting the PDMS bilayer with a scalpel in the central region, the gelatin swells and dissolves upon contact with the warm cell culture medium, releasing the pre-constraint and allowing for PDMS rolling. Thus, 2 symmetric tubes were produced per sample, kept in the incubator for defined timepoints after tube formation, and then fixed with 4% formaldehyde (PFA) in PBS for 20 min,

washed three times with PBS and kept in PBS at 4°C until imaging. In experiments where cell fixation was performed before cutting the substrate, samples were observed under the microscope at different timepoints after roll formation.

Cells on wavy substrates or on stretchers

After cells have been seeded and adhered until confluence to the prestressed and laser-treated elastomer films, the stretchers were brought back to a not-stressed position in order to produce the wrinkles in a few seconds and fixed in PFA at different timepoints as for the self-rolling substrates. For experiments where cells were compressed on flat elastomer films, cells were seeded on films pre-stretched by ~15 or 30%. The pre-stretch was rapidly released to induce compression, and cells were fixed in PFA at different timepoints as for the self-rolling substrates. For experiments where cells were stretched on flat elastomer films, cells were seeded on relaxed elastomer films mounted on stretchers, and rapidly stretched before fixation.

Hypo and hyper-osmotic treatments on flat substrates

Cells were observed at different timepoints after switching to a hypotonic (- ~155 mOsm) or hypertonic (+ ~510 mOsm) solution. Hypotonic solutions were prepared by adding double distilled water in the cell medium (1:1). Hypertonic conditions were obtained by replacing the cell medium by a a 0.5 M sucrose solution. Live imaging was performed in Leibovitz medium without phenol red (supplemented with 10% FBS, 1% PS, 1% NEAA).

Hyper-osmotic treatments on self-rolling substrates

Cells were incubated in hypertonic (+ ~600 mOsm, 0.5 M sucrose) solution after cutting the substrate and fixed at different timepoints in PFA with the same concentration of sucrose than in the hypertonic cell medium.

Flat surfaces for side views of actin labelling

10x2x2 mm PDMS parallelepipeds were glued by plasma activation on their largest side to the surface of glass-bottom dishes. These samples were used to culture cell monolayer at the surface of PDMS, and easily image their side view as in tubes, allowing for comparable measurements of actin intensity.

Drug treatments

Samples were incubated with drugs 30 min before cutting the substrates to produce the tubes and incubated in the medium with the drugs until fixation or before FLIM imaging, with the following concentrations: 100 μM DCPIB (100 mM stock solution in ethanol), 100 μM EIPA (100 mM stock solution in DMSO), 100 μM Bumetanide (100 mM stock solution in DMSO), 100 μM Furosemide (100 mM stock solution in DMSO), 200 nM Jasplakinolide (3 mM stock solution in DMSO), 20 μM Blebbistatin (17 mM stock solution in DMSO), 250 nM Torin1 (13mM stock solution in DMSO), 100 nM Rapamycin (1 mM stock solution in DMSO). For Latrunculin A (1 mM stock solution in DMSO), samples were incubated with the drug at 250 nM 20 min before cutting the substrates to produce the tubes and incubated in the medium with the drug until fixation. For PalmC (20 mM stock solution in DMSO), samples were incubated with the drug at 5 μM 7 min before cutting the substrates to produce the tubes and incubated in the medium with the drug until fixation or before FLIM imaging (except for live cells on the flat substrates where membrane tension and cell volume were observed before and after PalmC incubation).

Fluorescence labelling

After fixation, MDCK-II cells were stained with CellMask™ Deep Red Plasma Membrane Dye (1:1000) and nuclei were labelled with Hoechst 33342 (1:2000) for 15 min at room temperature.

F-actin was labelled on live MDCK-II cells with 1.3 μM SiR-Actin (1 mM stock solution in DMSO), incubated for 2 h. Cells were then fixed at different timepoints after cutting of the self-rolling substrates or after stretching/compression on flat elastomer films (see "Sample preparation").

For Ezrin immunostaining, after fixation, MDCK Myr-Palm-H2B cells were permeabilized using 0.1% saponin in PBS and blocked in 1% wt/vol fish gelatin solution in PBS for 45 min. Primary antibody mouse anti-Ezrin (1:200) was incubated for 1 h in 1% gelatin buffer. The secondary antibody donkey anti-mouse Alexa Fluor 488 (1:250) was incubated for 45 min in 1% gelatin buffer protected from light. Samples were washed three times with PBS after each antibody incubation. For phospho-Akt (ou p-Akt) immunostaining, MDCK-II cells were fixed with 4% PFA in PBS with 1X phosphatase inhibitor for 20min, washed three times with PBS. Then, cells were permeabilized using 0.01% Triton x100 in PBS and blocked in 3% wt/vol BSA solution in PBS for 1 h. Primary antibody rabbit anti-phospho-Akt (Ser473) (1:500) was incubated overnight in 3% BSA buffer at 4°C. The secondary antibody donkey anti-rabbit Alexa Fluor 488 (1:500) was incubated for 1 h in 3% BSA buffer protected from light. Finally, Hoechst 33342 was incubated 5 min to stain nuclei. Samples were washed three times with PBS after each antibody incubation. Phosphatase inhibitor 10X stock solution was kindly provided by N. Sen in R. Loewith lab at UniGe and prepared as following: 60 mM Sodium pyrophosphate tetrabasic decahydrate NaPPi, 100 mM Sodium fluorite NaF, 100 mM b-glycerophosphate disodium salt hydrate in water; pH was adjusted to 7.4 with 37% HCl and 124 mM 4-Nitrophenyl phosphate disodium salt hexahydrate pNPP was added to the final solution. FliptR probes were synthesized as previously reported (Dal Molin et al., 2015) or obtained commercially from Spirochrome (Flipper-TR, stock solution 1 mM in DMSO). 1 h before imaging (and before drug incubation, when relevant), MDCK-II cell medium was replaced with medium containing ~1 μM of FliptR.

Imaging

Fixed cells for volume quantification on PDMS tube samples and on flat substrates on the stretchers and with the wrinkles, E-cadherin MDCK fixed cells on PDMS tubes, live cells on flat substrates under hypoosmotic shocks and PDMS tubes without

cells for radius characterization (see "Image analysis") were imaged using an upright LSM 710 microscope with a water immersion Plan-Apochromat 20x/1.0 N.A. DIC objective (Carl Zeiss, Oberkochen, Germany), and operated with Zen 2012 software. Z-stack acquisitions were performed with Z-step of 0.5 μm for cell imaging and of 1 μm for imaging of PDMS tubes without cells. Tubes without cells were imaged in fluorescein dextran solutions. Confocal imaging of samples with actin-stained cells and immunostained samples with the phospho-Akt antibody, flat samples with live cells during osmotic shocks or drug treatments, and Fluorescence Lifetime Imaging (FLIM) for lifetime measurements were performed with an inverted Nikon Eclipse Ti A1R microscope equipped with a time-correlated single-photon counting module from PicoQuant GmbH (Berlin, Germany). Excitation for FLIM was performed as described previously (Colom et al., 2018) using a pulsed 485 nm laser (PicoQuant, LDH-D-C-485) operating at 20 MHz, and the emission signal was collected through a 600/50 nm bandpass filter using a gated PMA hybrid 40 detector and a TimeHarp 260 PICO board (PicoQuant). A water immersion Apo LWD 40X/1.15 N.A. objective (Nikon, Tokyo, Japan) was used for imaging of actin-stained and phospho-Akt-immunostained cells and FLIM acquisitions. A Plan Apo Lambda 100X/1.45 N.A. oil immersion objective (Nikon, Tokyo, Japan) was used for imaging of live cells on flat substrates under hyperosmotic shocks or drug treatment (PalmC and Latrunculin A) for cell volume quantification. Z-stack acquisitions were performed with a Z-step of 0.6 μm. Confocal imaging of actin-stained cells and Fluorescence Lifetime Imaging (FLIM) for lifetime measurements on the stretcher experiments were performed with an upright Leica SP8 LIVE FALCON microscope with a water immersion HC FLUOTAR 25X/0.95 N.A. objective (Leica, Wetzlar, Germany), and operated with LAS-X 2021 software. During live imaging, cells were maintained at 37°C with 5% CO_2 with a micro-incubator for thermal, CO_2 and humidity control (Okolab, Pozzuoli NA, Italy).

Confocal images of immunostained samples with the anti-Ezrin antibody were obtained using Nikon Eclipse Ti microscope with an Andor Zyla sCMOS camera with 60X Apochromat TIRF /1.49 N.A. DIC oil immersion objective (Nikon, Tokyo, Japan). The microscope was operated with SlideBook software. Z-stack acquisitions were performed with a Z-step of 0.3 μm.

QUANTIFICATION AND STATISTICAL ANALYSIS

Segmentation and cell volume quantification
Imaris 8.4.2 software (surface package) was used to segment fluorescent nuclei labelled with Hoechst or H2B-mCherry and calculate their centroid positions. To remove cells from the Z-stack edges that may have been partly cut, nuclei which position was equal or lower than 7 μm from the image border were removed from the statistics. The centroid positions were then used as seeds for the segmentation in 3D of Z-Stacks of MDCK-II cells labelled with the plasma membrane marker CellMask[TM] or Myr-Palm-GFP, and using LimeSeg (Machado et al., 2019) plugin on FijiJ. Possible systematic errors due to reconstruction from confocal imaging were estimated to be always lower than 11% (Roffay et al., 2021).

Actin intensity quantification
Icy software (point 2D tool) was used to select the regions of interest (ROI) of the apical and of the basolateral F-actin signal in order to quantify its intensity ratio.

p-Akt intensity quantification
A home-made plugin on FijiJ was used to select the nuclei with a threshold on the fluorescence intensity of the Hoechst channel, which was converted as a mask and used as a ROI selection on the p-Akt channel to firstly quantify the intensity in the nuclei and then, its inverse was used for the intensity quantification in the cytosol region.

Curvature quantification of PDMS tubes and wavy substrates
Radii of curvature were measured on self-rolling and wavy substrates at the PDMS surface where cells were supposed to adhere. On orthogonal views of the substrates, the chord of the arc (W) given by the PDMS substrate and the perpendicular bisector length (H) from the arc-chord were measured with the straight line tool in ImageJ. According to the chord theorem, the radius values

(R) were then calculated as $R = \dfrac{H}{2} + \dfrac{W^2}{8H}$.

Fluorescence lifetime analysis
SymPhoTime 64 software (PicoQuant) was used to fit fluorescence decay data (from regions of interest, ROI) with a double exponential function, where the background was set to "0" value, and the intensity weighted average lifetime was extracted. Independent replicates (N) represent repeated experiments that include 3 samples per timepoint or condition and usually 1 or 2 images are acquired on each tube (or flat region) on the sample.